Title

Manganese co-localizes with calcium and phosphorus in Chlamydomonas acidocalcisomes and is mobilized in manganese-deficient conditions

Journal

Journal of Biological Chemistry, 294(46)

ISSN

0021-9258

Authors

Tsednee, Munkhtsetseg
Castruita, Madeli
Salomé, Patrice A
et al.

Publication Date

2019-11-01

DOI

10.1074/jbc.ra119.009130

Peer reviewed

Manganese co-localizes with calcium and phosphorus in *Chlamydomonas* acidocalcisomes and is mobilized in manganese-deficient conditions

Received for publication, April 29, 2019, and in revised form, September 9, 2019 Published, Papers in Press, September 16, 2019, DOI 10.1074/jbc.RA119.009130

Munkhtsetseg Tsednee[‡1], Madeli Castruita[‡1], Patrice A. Salomé[‡§1], Ajay Sharma[¶], Brianne E. Lewis[‖], Stefan R. Schmollinger[‡§2], Daniela Strenkert[‡§3], Kristen Holbrook[‡4], Marisa S. Otegui[**], Kaustav Khatua[‡‡], Sayani Das[‡‡], Ankona Datta[‡‡], Si Chen[§§], Christina Ramon[¶¶], Martina Ralle[‖‖], Peter K. Weber[¶¶], Timothy L. Stemmler[‖], Jennifer Pett-Ridge[¶¶], Brian M. Hoffman[¶], and Sabeeha S. Merchant[‡§5]

From the [‡]Department of Chemistry and Biochemistry and [§]Institute for Genomics and Proteomics, UCLA, Los Angeles, California 90095, the [¶]Department of Chemistry, Northwestern University, Evanston, Illinois 60208, the [‖]Department of Pharmaceutical Sciences, Wayne State University, Detroit, Michigan 48201, the [**]Departments of Botany and Genetics, University of Wisconsin, Madison, Wisconsin 53706, the [‡‡]Department of Chemical Sciences, Tata Institute of Fundamental Research, Mumbai 400005, India, the [§§]Advanced Photon Source, Argonne National Laboratory, Lemont, Illinois 60439, the [¶¶]Physical and Life Sciences Directorate, Lawrence Livermore National Laboratory, Livermore, California 94550, and the [‖‖]Department of Molecular and Medical Genetics, Oregon Health and Science University, Portland, Oregon 97239

Edited by Phyllis I. Hanson

Exposing cells to excess metal concentrations well beyond the cellular quota is a powerful tool for understanding the molecular mechanisms of metal homeostasis. Such improved understanding may enable bioengineering of organisms with improved nutrition and bioremediation capacity. We report here that *Chlamydomonas reinhardtii* can accumulate manganese (Mn) in proportion to extracellular supply, up to 30-fold greater than its typical quota and with remarkable tolerance. As visualized by X-ray fluorescence microscopy and nanoscale secondary ion MS (nanoSIMS), Mn largely co-localizes with phosphorus (P) and calcium (Ca), consistent with the Mn-accumulating site being an acidic vacuole, known as the acidocalcisome. Vacuolar Mn stores are accessible reserves that can be mobilized in Mn-deficient conditions to support algal growth. We noted that Mn accumulation depends on cellular polyphosphate (polyP) content, indicated by 1) a consistent failure of *C. reinhardtii vtc1* mutant strains, which are deficient in polyphosphate synthesis, to accumulate Mn and 2) a drastic reduction of the Mn storage capacity in P-deficient cells. Rather surprisingly, X-ray absorption spectroscopy, EPR, and electron nuclear double resonance revealed that only little Mn^{2+} is stably complexed with polyP, indicating that polyP is not the final Mn ligand. We propose that polyPs are a critical component of Mn accumulation in Chlamydomonas by driving Mn relocation from the cytosol to acidocalcisomes. Within these structures, polyP may, in turn, escort vacuolar Mn to a number of storage ligands, including phosphate and phytate, and other, yet unidentified, compounds.

In algae and land plants, manganese (Mn)[6] is the cofactor for at least 30 enzymes: phosphoenolpyruvate carboxylase and oxalate oxidase among others (1–3). By far, the two major Mn sinks in the green lineage are the various Mn-containing superoxide dismutases (MnSODs)[7] distributed in the cytosol, mitochondria, and plastids (4–6) and photosystem II in chloroplasts. MnSOD protects against superoxide (generated in the bioenergetic membranes of photosynthesis and respiration among other metabolic reactions), whereas PSII houses the water oxidation complex in photosynthesis (7). Mn is therefore a key nutrient for plants and algae, with a quota typically much higher than in animals and respiring bacteria.

Although iron (Fe) and Mn are two of the most abundant transition metals in the Earth's crust, the rise in oceanic oxygen

This work was supported by the Division of Chemical Sciences, Geosciences, and Biosciences, Office of Basic Energy Sciences of the United States Department of Energy (Grant DE-FG02-04ER15529). This work was also supported by DOE Genome Sciences Program Grant SCW1039 (to C. R., S. R. S., P. K. W., and J. P.), National Science Foundation Grant MCB1614965 (to M. S. O.), and National Institutes of Health Grants DK068139 (to T. L. S.), T32HL120833 (to B. E. L.) and GM 111097 (to B. M. H.). The authors declare that they have no conflicts of interest with the contents of this article. The content is solely the responsibility of the authors and does not necessarily represent the official views of the National Institutes of Health.

This article contains Figs. S1–S14.

[1] These authors contributed equally to this work.

[2] Present address: 427 Stanley Hall QB3, UC Berkeley, Berkeley, California 94720.

[3] Present address: 427 Stanley Hall QB3, UC Berkeley, Berkeley, California 94720.

[4] Present address: Amgen, 1 Amgen Center Dr., Thousand Oaks, CA 91320.

[5] To whom correspondence should be addressed: 176 Stanley Hall QB3, UC Berkeley, Berkeley, CA 94720. E-mail: sabeeha@chem.ucla.edu.

[6] Throughout the text, we use the elemental symbol (Mn, Fe, etc.) as an abbreviation of the word when we are referring generically to all species of a given element; we indicate the ionic species only when referring to a specific ionic form.

[7] The abbreviations used are: SOD, superoxide dismutase; PSII, photosystem II; XANES, X-ray absorption near edge structure; nanoSIMS, nanoscale secondary ion MS; XFM, X-ray fluorescence microscopy; EDX, energy-dispersive X-ray spectroscopy; polyP, polyphosphate; TEM-EDX, transmission EM coupled with energy-dispersive X-ray spectroscopy; VTC, vacuolar transporter chaperone complex; TEM, transmission EM; EXAFS, extended X-ray absorption fine structure; ENDOR, electron nuclear double resonance; ESEEM, electron spin echo envelope modulation; kG, kilogauss; Phy, phytate; TAP, Tris-acetate-phosphate; TA, Tris acetate; STEM, scanning transmission EM; ROI, region of interest; DAPI, 4′,6-diamidino-2-phenylindole; Sc, calibrated scale factor.

from oxygenic photosynthesis caused their massive precipitation as oxide complexes: their availability dropped by orders of magnitude (2 for Mn, and 4 for Fe), placing tremendous pressure on early unicellular organisms to meet their transition metal quotas for enzymes that had incorporated Fe or Mn cofactors (8) and presumably providing the driving force for the evolution of metal-selective transporters and intracellular metal sequestration mechanisms.

Mn and Fe deficiency are symptomatically similar in plants, as they both decrease the efficiency of photosynthesis and are both accompanied by leaf chlorosis (9), although the underlying causes are different. In the case of Fe, chlorosis results from inhibition of chlorophyll biosynthesis (10), now attributed to the di-iron cyclase in the pathway (11), and also from programmed reorganization of the photosynthetic apparatus for photoprotection and iron sparing (12–15). Mn deficiency likely destabilizes the PSII complex, perhaps due to the release of the extrinsic lumenal proteins (5). Mn deficiency also increases intracellular redox stress because of decreased SOD activity, which manifests as necrotic regions on leaves (3, 16) or replacement of Mn in enzymes with Fe (17).

On the other end of the nutrient assimilation spectrum, excess Fe or Mn can be detrimental for growth, although for different reasons. High cellular Fe levels generate reactive oxygen species via the Fenton reaction, whose toxicity is exacerbated under high photon flux densities (18). For Mn, there is the danger of mismetalation and potential inactivation of the substituted metalloenzyme (17). Two notable exceptions are the budding yeast and the bacterium *Deniococcus radiodurans*. In both organisms, high concentrations of cellular Mn help protect proteins against oxidative stress damage due to the high superoxide dismutation activity displayed by Mn-phosphate low-molecular weight metabolites (19–21).

To prevent experiencing either metabolic extreme, all living organisms have devised elaborate systems for the uptake, transport, storage, and remobilization of micronutrients. Mn is typically transported as Mn^{2+} species, often by members of the same transporter families that transport Fe^{2+}. These transporters include members of the NRAMP (natural resistance-associated macrophage protein), MTP (metal tolerance protein), and VIT1/CCC1 (vacuolar iron transporter in *Arabidopsis*) families (16, 22–27). Primary Mn^{2+} uptake takes place at the plasma membrane by NRAMPs and is subsequently routed to the endoplasmic reticulum, Golgi, mitochondria, and chloroplasts (in algae and plants) to fulfill the metalation needs of each compartment. In addition, cells can store Mn^{2+} in vacuoles for later use under conditions of nutrient limitation or to minimize the toxic effects of overaccumulation when placed in an environment with an overabundance. In this regard, the vacuole acts as a temporary cellular sponge for excess Mn^{2+} (this work).

Because Mn^{2+} and Fe^{2+} can be transported by the same transporters, a greater understanding of Mn metabolism is relevant not only for appreciating Mn biochemistry but also for a systems-level view of Fe homeostasis that includes potential cross-talk and interactions with other metals. For instance, high Mn availability can induce Fe-deficiency symptoms (28, 29) by competing for the same transporters (22, 30–32). The Arabidopsis high-affinity Mn^{2+} transporter NRAMP1 can also function as a low-affinity Fe^{2+} transporter under Fe-replete conditions (33). Yet, despite its critical function in photosynthesis, Mn metabolism is underinvestigated. In the unicellular alga *Chlamydomonas reinhardtii* (hereafter referred to as Chlamydomonas), Mn deficiency strongly induces the expression of *NRAMP1* and can also be associated with secondary Fe deficiency (5). The effects of high Mn supply in Chlamydomonas are unknown.

High concentrations of Mn in the soil typically rise after heavy rains and are exacerbated in acid soils. The analysis of various yeast mutants pointed to a role for phosphate in Mn uptake, perhaps as a co-transported counterion on phosphate transporters (21, 34–36). Polyphosphate chains are also critical for magnesium (Mg^{2+}) uptake, suggested to act as a cation filter that attracts Mg^{2+} to the vacuole (37). It is becoming more appreciated that lysosome-type organelles (of which the vacuole is one), called acidocalcisomes (because of their low pH and high calcium content), are key sites for metal storage (38–41).

We tested the metal content of Chlamydomonas as a function of Mn^{2+}-EDTA supply in the medium. Surprisingly, we found that cells accumulate Mn^{2+} in linear proportion to supply many times over their demands for metalating all Mn sites in proteins (also referred to as quota). Spectroscopic analysis (X-ray absorption near edge structure; XANES) indicates that intracellular Mn is mostly present as Mn^{2+} species, as expected. Based on various imaging methods, including nanoscale secondary ion MS (nanoSIMS), scanning X-ray fluorescence microscopy (XFM), energy-dispersive X-ray spectroscopy (EDX), and fluorescence imaging, we conclude that Mn^{2+} is concentrated in the acidocalcisome. Mutants blocked in polyphosphate (polyP) synthesis do not accumulate Mn^{2+}. However, spectroscopic studies (extended X-ray absorption fine structure (EXAFS) and electron nuclear double resonance (ENDOR)) do not support Mn^{2+} association with polyP. Therefore, we conclude that polyP functions as an escorting and temporary ligand within acidocalcisomes rather than an end-point sequestration agent as suggested for Mg ions (37).

Results

Chlamydomonas cells have a linear capacity for Mn accumulation

Mn deficiency in Chlamydomonas is associated with slow growth and decreased chlorophyll content due to compromised photosynthetic electron transfer (5). To determine the behavior of Chlamydomonas cells under conditions of Mn excess, we exposed cultures to Mn concentrations ranging from 6 to 1000 μM and monitored growth, chlorophyll levels, and photosynthetic parameters. All Mn concentrations were well-tolerated by Chlamydomonas and even provided an apparent growth advantage at 50 μM and above (Fig. 1*A*). Higher concentrations of cellular Mn may participate in quenching of reactive oxygen species harmful to cells, as was shown in yeast (20, 42). All cultures were healthy, as demonstrated by robust chlorophyll accumulation and F_v/F_m values, with no indication of cellular stress (Fig. S1). Other metals like Fe, copper (Cu), zinc (Zn), and phosphorus (P) remained constant over the range of Mn concentrations tested here, with the exception of a slight

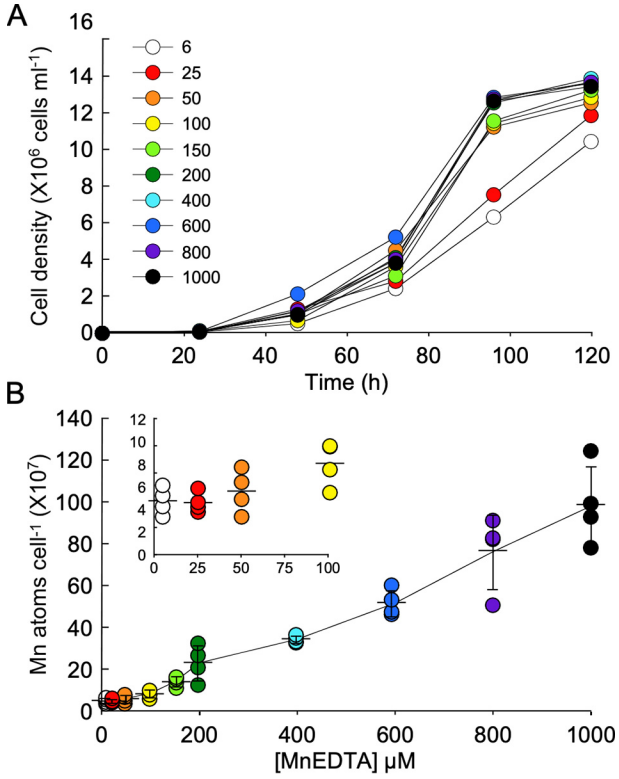

Figure 1. Chlamydomonas cells accumulate Mn under excess. Cultures were inoculated from a 6 μM MnEDTA preculture at an initial cell density of 10^4 cells ml^{-1} and grown in medium supplied with the indicated amount of MnEDTA (photon flux density, ~100 μmol m^{-2} s^{-1}). *A*, growth was measured by counting cells every 24 h in a hemocytometer. *B*, intracellular Mn content was quantified via ICP-MS from four independent experiment replicates. The *horizontal bars* represent the mean for each sample ± S.D. (*error bars*).

increase in intracellular calcium (Ca) under very high Mn concentrations (Fig. S2).

The observed tolerance to excess external Mn was accompanied by intracellular accumulation of the metal well beyond its normal quota (Fig. 1*B*). Chlamydomonas cells indeed displayed a linear capacity for Mn uptake from the medium that was not saturated even at 1 mM Mn. This behavior is unique among the metals we have tested and suggests that a distinct control mechanism operates for Mn^{2+} uptake and storage. Indeed, we have previously observed rapid saturation of Cu uptake that does not extend beyond 2–3 × 10^7 atoms/cell (41, 43). The Fe quota is much higher, and its accumulation continues even after the quota is reached, but nevertheless more slowly (13).

We conclude that Chlamydomonas cultures exhibit a linear capacity for Mn uptake to many times its normal quota for photosynthesis and that this intracellular accumulation appears to be beneficial to cell growth.

Mn co-localizes with Ca and P inside acidocalcisomes

In Arabidopsis, the major Mn storage site is the vacuole, from which it can be remobilized by NRAMP family members (16, 22, 44). We explored intracellular Mn distribution in Chlamydomonas cells grown in Mn-replete and excess conditions by multiple techniques: XFM, transmission EM coupled with energy-dispersive X-ray spectroscopy (TEM-EDX), and nanoSIMS. Each method offers particular advantages, and all three were largely congruent; we present the results from nanoSIMS below. XFM and TEM-EDX are shown in Figs. S3 and S4.

NanoSIMS is a method that maps elements, in surfaces of solid samples based on their mass with high spatial resolution. The method is compatible with visualizing populations of cells, which enables statistical analysis of regions of interest. In conjunction with the use of standards, quantitative information can be extracted from the data. Fixed cells grown in 6 or 1000 μM MnEDTA were analyzed with an O^- analysis beam, and secondary ions were collected for carbon ($^{12}C^+$), phosphorus ($^{31}P^+$), calcium ($^{40}Ca^+$), and manganese ($^{55}Mn^+$). We report elemental abundances as uncorrected ion ratios, as reflected by the specific isotope species detected. As shown in Fig. 2*A*, P, Ca, and Mn showed clear co-localization in a field of cells grown in excess Mn. XFM observations of fixed whole cells painted a similar picture of intracellular metal distribution (Fig. S3). Sites of P and Ca accumulation coincide with electron-dense particles seen by TEM-EDX (Fig. S4) and are consistent with the defining elemental content of the acidocalcisome, a lysosome-related organelle. We exploited the sensitivity and dynamic range of nanoSIMS to quantify relative P, Ca, and Mn levels by subdividing each cell into nonoverlapping regions of interest (see Fig. S5) and normalizing ion counts to $^{12}C^+$ (41). We used the sites of high $^{40}Ca^+/^{12}C^+$ and $^{31}P^+/^{12}C^+$ concentration as proxy for acidocalcisomes (Fig. 2, *B* and *C*). The relative concentration of Ca and P did not change inside acidocalcisomes as a function of Mn supply (Fig. S6). However, Mn accumulation in cells exposed to excess MnEDTA was 100-fold higher than in cells supplied with 6 μM MnEDTA and coincided with foci of high Ca (Fig. 2*B*) and P (Fig. 2*C*). Because regions of interest were drawn randomly within cellular sections, they did not perfectly overlap with P, Ca, and Mn (see Fig. S5). Nevertheless, $^{55}Mn^+/^{12}C^+$ correlated positively with $^{40}Ca^+/^{12}C^+$ ($R^2 = 0.76$) and $^{31}P^+/^{12}C^+$ levels ($R^2 = 0.67$) under excess-Mn conditions. The relative concentrations of all three elements co-varied linearly over a 100-fold range. To further illustrate these relationships, we selected 10 Mn foci and four low-Mn regions and determined associated Ca and P levels (shown as *red* and *blue circles* in Fig. 2, *B* and *C*). We note that a small Mn fraction may remain in the cytosol of cells grown under Mn excess, where it does not co-localize with Ca or P foci (*blue circles*). At these locations, Mn levels were still higher than within most Ca foci in cells grown under normal Mn supply. These results, obtained from three independent imaging techniques, therefore collectively demonstrate sequestration of Mn into the P- and Ca-rich acidocalcisomes, over a wide range of Mn concentrations in the growth medium.

A mutant in the VTC complex does not accumulate manganese

Based on the yeast literature on manganese metabolism, and in view of its concentration within acidocalcisomes, we hypothesized that Mn ions were stored inside the organelle complexed with polyP (45, 46). The vacuolar transporter chaperone (VTC) complex catalyzes the synthesis of polyP from cytosolic P_i and translocates the polymer across the vacuolar membrane in an ATP-dependent manner. The VTC complex is composed of five subunits in yeast, Vtc1–Vtc5 (35, 47). The Chlamydomonas

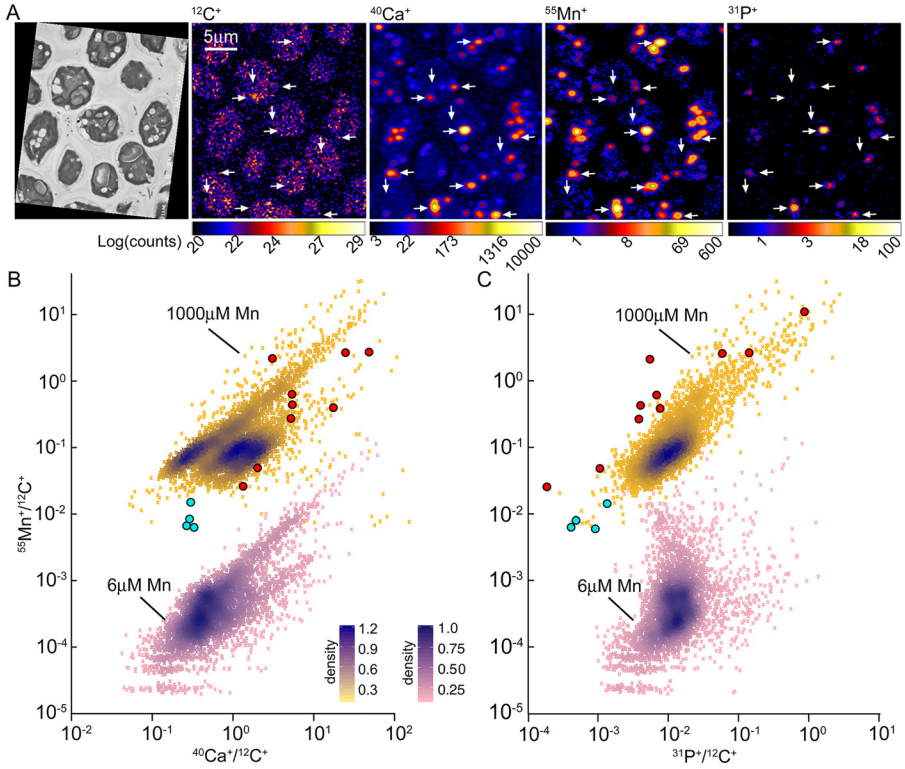

Figure 2. Correlative quantification of $^{12}C^+$-normalized $^{55}Mn^+$ with $^{31}P^+$ and $^{40}Ca^+$ shows co-localization of Mn with Ca and P. *A*, correlated STEM and nanoSIMS imaging of cells grown in medium containing 1000 μM Mn. Sections of fixed Chlamydomonas cells were imaged in positive secondary ion mode. *Scale bar*, 5 μm. *B* and *C*, correlative quantification of $^{12}C^+$-normalized $^{55}Mn^+$ with $^{31}P^+$ and $^{40}Ca^+$ from nanoSIMS imaged cells grown in 1000 μM (three replicates) and 6 μM MnEDTA (two replicates). The subcellular correlation of ROIs for $^{55}Mn/^{12}C$ *versus* $^{40}Ca/^{12}C$ is shown in *B*, and that for $^{55}Mn/^{12}C$ *versus* $^{31}P/^{12}C$ is shown in *C*. *Arrows*, regions of high (← and →) and low (↓) concentration of Mn, Ca, and P in the nanoSIMS image for each element; the same areas of interest are shown as *red dots* (high) and *blue dots* (low), respectively, in the correlation plots in *B* and *C*.

genome encodes one orthologue for Vtc1 and Vtc4 each, and a mutant in *VTC1*, lacking detectable polyP, is available for phenotypic characterization (48). Growth of the *vtc1-1* mutant was not adversely affected by excess Mn (Fig. 3*A*), yet a role for polyP in Mn accumulation became evident when we determined the elemental profiles of *vtc1-1 versus VTC1* complemented strains cultured in medium with varied Mn content. The complemented strain accumulated Mn with the same linear capacity as did the WT laboratory strain CC-4532, with an 11-fold increase in Mn content between 6 and 600 μM (Figs. 1*B* and 3*B*). This capacity was greatly reduced in the *vtc1-1* mutant: starting with only half of the Mn content normally seen in *VTC1*, the mutant managed only a 2-fold rise in its Mn content, even when supplied with 600 μM MnEDTA (Fig. 3*B*). Other elements that differentiated *VTC1* and *vtc1-1* included P (Fig. 3*C*) and Ca (Fig. 3*D*); neither element content changed as a function of Mn supply in either genotype, but P levels in *vtc1-1* were one-third of those in *VTC1*, whereas Ca levels reached at most one-tenth of those in *VTC1*, suggesting that Ca ions may associate directly with polyP. That *vtc1-1* mutants have a lower P quota is expected, as vacuolar polyP makes a substantial contribution to the total cellular P content in WT cells, equivalent to molar concentrations of P inside acidocalcisomes (49). The elemental profile of the Chlamydomonas *vtc1-1* mutant is in line with the yeast *vtc1* mutant, which has an even more pronounced decrease in internal P content (50).

If the lower Ca content of *vtc1-1* were responsible for its inability to accumulate Mn, then growing WT cells with a fraction of the Ca normally supplied in our standard growth medium (340 μM) should phenocopy the *vtc1-1* mutant phenotype. However, we did not discern any drop in Mn accumulation, even when the Ca supply was reduced to only 10% of normal levels, leading to a ~60% reduction in cellular Ca (Fig. S7, *A* and *B*). Cellular P contents only decreased slightly at the lowest Ca supply levels (Fig. S7*C*). In contrast, withholding P from the growth medium, which resulted in a 40-fold drop in cellular P levels (Fig. S8), did interfere with both Mn and Ca accumulation. Indeed, P-limited cells only contained one-quarter of the Mn taken up by P-replete cells when exposed to excess Mn (Fig. S8*A*); their Ca content was also very low and reminiscent of Ca levels in *vtc1* mutants (Fig. 3*D* and Fig. S8*C*). By similarity with *Escherichia coli* and yeast, we hypothesize that P limitation is accompanied by a severe drop in polyP that would prevent Mn (and Ca) accumulation, in agreement with our results with the *vtc1-1* mutant (Fig. 3). As shown recently for Mg ions (37), polyP therefore also plays a crucial role in Mn and Ca accumulation inside acidocalcisomes.

Aksoy *et al.* (48) reported that acidocalcisomes were missing in *vtc1-1*, which would easily explain the loss of Mn accumulation in the mutant. However, their conclusion relied on identifying acidocalcisomes as electron-dense particles in TEM images (48). Such particles inside acidocalcisomes are likely polyP crystals (49, 51, 52). *vtc* mutants do not accumulate polyP in yeast (35) or Chlamydomonas (48), and we wondered whether the presented evidence for the lack of acidocalcisomes in the *vtc1-1* mutant might be inconclusive. We therefore used

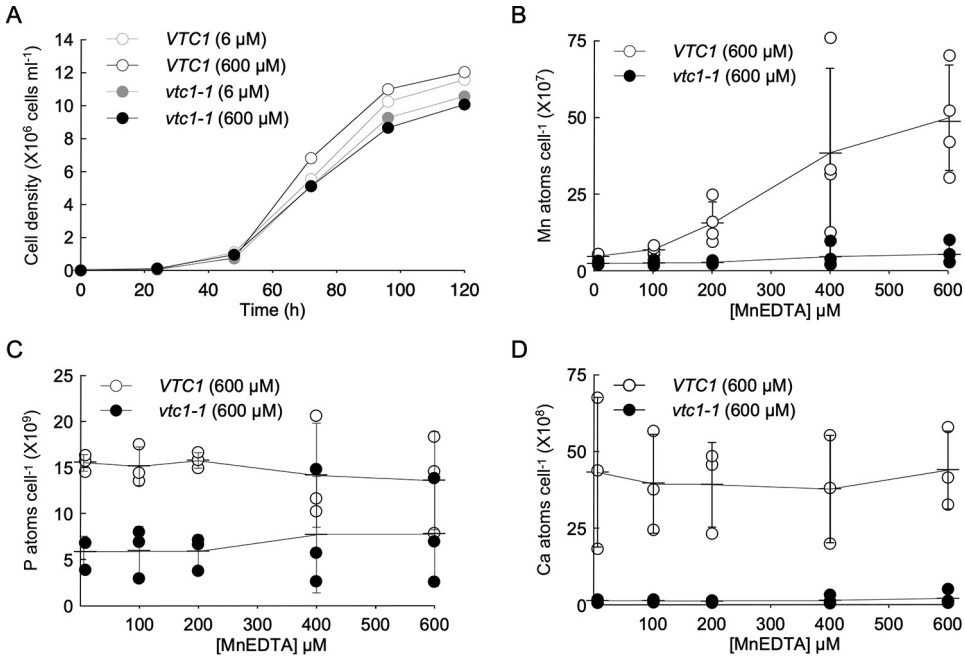

Figure 3. *vtc1-1* mutant defective in polyphosphate and Ca accumulation does not accumulate Mn under excess-Mn condition. Cultures of the complemented strain (*VTC1*) and *vtc1-1* mutant were inoculated into medium containing 6 or 600 μM MnEDTA with an initial cell density of 10^4 cells ml^{-1} (photon flux density, ~100 μmol m^{-2} s^{-1}). *A*, growth was measured by counting cells every 24 h in a hemocytometer. Total Mn (*B*), P (*C*), and Ca (*D*) content was measured by ICP-MS from four independent experiment replicates. The *horizontal bars* represent the mean for each sample ± S.D. (*error bars*).

the lysosensor dye DND189, which is used to visualize acidic organelles like lysosomes and acidocalcisomes. We observed many small acidic compartments in *VTC1* and *vtc1-1* cells grown under both standard conditions and Mn excess, which argues that the *vtc1* mutant can generate a significant proton gradient across the acidocalcisome membrane (Fig. 4, *A* and *B*). Staining of polyP with DAPI was only positive in *VTC1*, as described previously (Fig. 4 (*C* and *D*); see Aksoy *et al.* (48)). The inability of *vtc1-1* to accumulate Mn thus cannot be attributed trivially to a loss of acidocalcisomes in the mutant and points to another process that is impaired.

To determine whether the acidocalcisome membrane was compromised in the absence of VTC1, we searched for the vacuolar membrane proteins H^+-pyrophosphatase and V-ATPase in a proteomics data set performed in another *vtc1* allele (*vtc1-2*, with similar defects in P, Ca, and Mn accumulation as *vtc1-1*; Fig. S9*A*) and its associated WT strain CC-4533. We detected comparable spectral counts for the H^+-pyrophosphatase and all subunits of the V-ATPase in *vtc1-2* and its WT strain (Fig. S9*B*), which is consistent with the presence of an organelle with a functional and energized boundary membrane (as noted from lysosensor DND189 staining, mentioned above). These results also argue that although the yeast and Chlamydomonas *vtc1* mutants are phenotypically close in terms of their elemental profile (Fig. 3; Yu *et al.* (50)), they are not biochemically identical. Indeed, the yeast *vtc1* mutant is distinct in that it causes a general drop in the levels of several V-ATPase subunits at the vacuolar membrane (47), and the locus is named for that phenotype (vacuolar transporter chaperone). Also not observed in the Chlamydomonas *vtc1* mutant was a large change in the levels of the H^+-pyrophosphatase or in the predicted homologues to the yeast membrane H^+-ATPase Pma1p

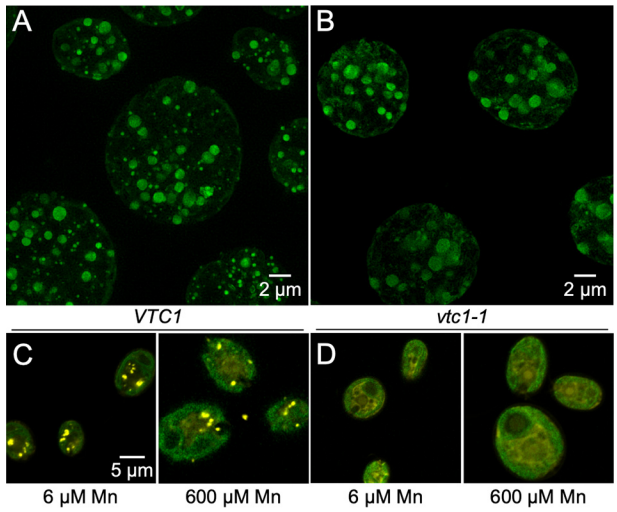

Figure 4. *vtc1-1* mutant cells contain an acidic compartment. The low-pH dye Lysosensor DND-189 can detect low-pH compartments in both *VTC1* (*A*) and mutant *vtc1-1* cells (*B*) using Zeiss Elyra Lattice SIM in channel mode. *VTC1* (*C*) and mutant *vtc1-1* cells (*D*) exposed to replete (6 μM) or high (600 μM) Mn were stained with phosphate dye (DAPI) to observe intracellular polyphosphate accumulation (which appears *yellow* when present). Chlorophyll autofluorescence is shown in *green*. Confocal images were collected on a Zeiss 880 microscope using Airyscan in channel mode, and exposures were adjusted as needed to observe intracellular staining. *Scale bar*, 5 μm. Images are representative of one replicate for each condition.

(Fig. S9*C*). We did, however, detect fewer peptides for the VTC4 subunit of the VTC complex in the mutant, as might be expected when a multisubunit protein complex is missing a component. Although we cannot rule out more minute changes in the levels or localization of vacuolar membrane proteins in the Chlamydomonas *vtc1* mutant, we conclude that the acidocalcisome boundary membrane is largely functional.

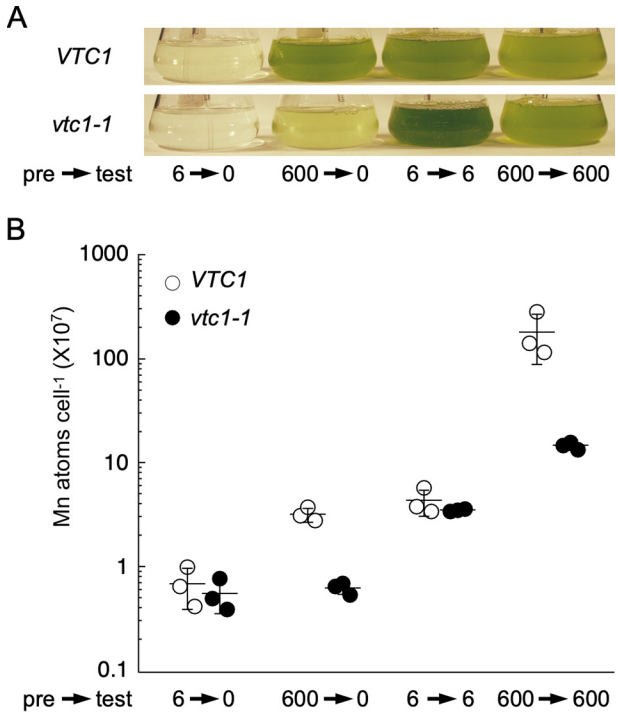

Figure 5. Accumulated Mn can be used as a reservoir under low-Mn condition. Precultures and test cultures of the *vtc1-1* mutant and complemented strain (*VTC1*) were grown in a minimal growth medium (−*acetate*) with air bubbling. Pretest cultures were grown with 6 or 600 μM Mn for 1 week. Test cultures were inoculated with EDTA-washed cells with different Mn concentration (no added Mn, 6 and 600 μM MnEDTA) and grown for 7 days. *A*, representative photographs of flasks for *VTC1* and *vtc1-1* after 6 days of growth in absence of added Mn, after pretreatment with 6 or 600 μM MnEDTA. *B*, total Mn content of *VTC1* and *vtc1-1* cells shown in *A*. The *horizontal bars* represent the mean for each sample ± S.D. (*error bars*) (n = 3). The experiment was repeated three times with similar results.

Mobilization of stored Mn when challenged by Mn deficiency

It is well-established that cells will prioritize particular metalloenzymes when faced with a limited metal supply (43, 53). Although *vtc1* mutants only accumulate one-third of the Mn normally seen in WT cells under standard growth conditions (Fig. 3 and Fig. S9*A*), they show no signs of Mn deficiency, and Mn-containing proteins are just as abundant in the *vtc1* mutant as they are in the WT strain (Fig. S9*C*). We therefore asked whether the Mn pool that accumulates in WT cells was biologically accessible. Accordingly, we first grew *vtc1-1* and *VTC1* strains photoautotrophically in 6 and 600 μM MnEDTA and washed cells with EDTA to remove trace metals from the cell surface before transferring them to fresh medium with no added Mn. We chose photoautotrophic conditions to place stronger pressure on the photosynthetic apparatus, the main Mn sink with an essential function in photosynthetic cells, to more easily discern a phenotype (54). Indeed, the growth potential of Chlamydomonas cells was determined by the genotype at the *VTC1* locus and by prior exposure to excess Mn. *VTC1* cultures grew well if the inoculum originated from a 600 μM MnEDTA preculture, but not from a 6 μM MnEDTA preculture (Fig. 5*A*). The elemental profile for Mn across conditions confirmed Mn accumulation in *VTC1* cells grown in 600 μM MnEDTA at all times. This stored Mn was sufficient to sustain growth for at least 1 week when cells were transferred to growth medium with no added Mn, demonstrating that it was biologically accessible under Mn limitation. The *vtc1-1* mutant presented an important control: in the absence of Mn accumulation typical for this mutant, cells could not survive unless provided with some MnEDTA in the growth medium, even when the preculture was exposed to 600 μM MnEDTA (Fig. 5*A*). This control also argues against the trivial explanation of Mn carryover from the pretreatment condition. Actively growing photosynthetic cells require 2–3 × 10^7 atoms of Mn/cell to perform adequately, and this held true in this experiment. Growth-arrested cells were well below this mark, with Mn levels closer to 0.5–0.7 × 10^7 atoms of Mn/cell (Fig. 5*B*). In summary, stored Mn from acidocalcisomes can be remobilized to sustain growth and photosynthesis when Chlamydomonas is challenged by Mn limitation.

Determination of Mn oxidation and speciation within acidocalcisomes

To validate the hypothesis that polyP was acting as the main Mn ligand by defining the complexation and speciation of cellular Mn, we applied XANES and EXAFS spectroscopies to probe nearest-neighbor and long-range metal-ligand environments. We focused on the Mn K-edge, during which a metal 1s core electron is promoted to a vacant 3d orbital (in the pre-edge region) or to the continuum for all metal collected from cells grown in excess Mn (1000 μM MnEDTA). As shown in Fig. 6*A*, all samples showed a limited pre-edge feature in the XANES, consistent with metal existing in an octahedral ligand symmetry (9, 55). The excitation edge for Mn in cells matched that from the $MnSO_4$ standard in both inflection energy and overall shape, indicating that, as expected, accumulated Mn was predominantly present in the low-oxidation Mn^{2+} species and not in a high-oxidation state.

Oscillations in an EXAFS spectrum are caused by scattering of the excited electron from the absorbing atom interacting with neighboring scattering atoms, the deconvolution of which provides a means to determine the distance between Mn and the neighboring atom and to estimate the chemical nature of this atom through simulation of a theoretical curve to the empirical data (56). Fourier transforms of EXAFS data provide a ~0.5 Å phase-shifted radial distribution function of the ligand environments around the absorbing metal (Fig. 6*B* (*right*, *top*, and *bottom*)), whereas simulations of the EXAFS data can be used to provide direct metrical details of the metal–ligand environment (Fig. 6*B* (*left*, *top*, and *bottom*)). The best-fit simulation results suggested a nearest-neighbor ligand environment consisting of 5–6 oxygen and/or nitrogen ligands (based on *error bars* of the data) at a distance of 2.18 ± 0.02 Å, whereas long-range scattering could be equally explained by 2–4 carbon (C) ligands or a single P ligand (around 4 Å from Mn atoms), with weaker support for P scattering (Table 1 and Fig. 6). A double peak between 2–4k was poorly explained by a fit with either C or P. Hydrated Mn Mn-$(H_2O)_6$ can exhibit such oscillations in the 2–4k range, especially at lower pH (9), which would be compatible with the acidic environment of the acidocalcisome. A contribution by an imidazole-containing ligand (*e.g.* histidine) is another (nonexclusive) possibility, as Mn-histidine complexes only display a single peak in the 2–4k range (9).

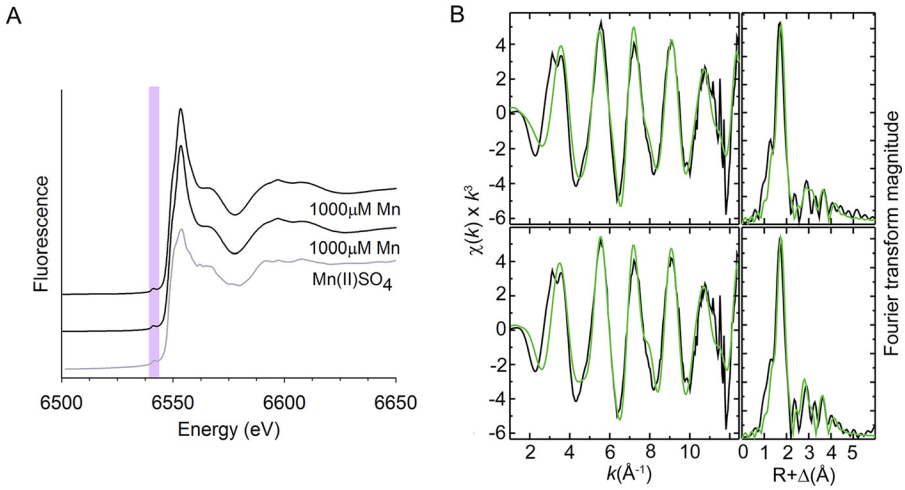

Figure 6. Accumulated Mn is a Mn^{2+} species predominantly associated with oxygen and nitrogen. *A*, Mn XANES were obtained from cells grown in medium containing 1,000 μM MnEDTA. Spectra with a pre-edge feature at 6,541.1 eV (shown in *lilac*) correspond to the 1s–3d transition. Comparisons of two sample duplicates (*black*) with a $MnSO_4$ standard (*gray*) represent Mn^{2+} species. The excess-Mn samples were offset from the standard. *B*, k^3-weighted EXAFS data (*left panels*) and phase-shifted Fourier transform (*right panels*) are shown for representative scans of raw unfiltered data (*black*) and best-fit simulations (*green*) from Mn-loaded cells. Near-neighbor ligand environments are primarily constructed of O/N, whereas mixed scattering was observed in the long-range ligand environment for both P and C. EXAFS data for the long-range ligand environment corresponding to P is shown in *B* (*top*) and for C in *B* (*bottom*).

Table 1

Summary of Mn EXAFS fitting analysis for 1000 μM Mn Chlamydomonas cell samples

EXAFS fitting analysis was done for two independent sample replicates: 1,000 μM Mn(1) and 1,000 μM Mn(2). Long-range scattering could be best fit using carbon scattering (Solution 1) with F' values of 0.85 and 1.02 for each replicate or including phosphorus scattering (Solution 2) with F' values of 0.78 and 1.02.

Sample	Nearest-neighbor ligand environment[a]				Long-range ligand environment[a]				
	Atom[c]	R^d	CN[e]	σ^{2f}	Atom[b]	R^d	CN[e]	σ^{2f}	F'^b
		Å				Å			
Solution 1: Fit to C									
1000 μM Mn(1)	O/N	2.18	5	4.93	C	3.22	4	2.52	0.85
					C	3.94	3	1.86	
					C	4.45	4	1.66	
1000 μM Mn(2)	O/N	2.18	5	4.01	C	3.22	4	1.82	1.02
					C	3.97	4	1.26	
					C	4.46	3	2.48	
Solution 2: Fit to P									
1000 μM Mn(1)	O/N	2.18	5	5.11	P	3.34	1	1.59	0.78
					C	3.95	2	1.01	
					C	4.46	4	2.47	
1000 μM Mn(2)	O/N	2.18	5	4.18	P	3.34	1	1.53	1.02
					C	3.98	4	2.03	
					C	4.49	3	2.08	

[a] Independent metal-ligand scattering environment.
[b] Number of degrees of freedom weighted mean square deviation between data and fit.
[c] Scattering atoms: N (nitrogen), O (oxygen), C (carbon), and P (phosphorus).
[d] Average metal–ligand bond length, ± 0.13 $Å^{-1}$.
[e] Average metal–ligand coordination number (CN) ± 1.0.
[f] Average Debye–Waller factor (Å × 10^3).

We next employed EPR, ENDOR, and electron spin echo envelope modulation (ESEEM) spectroscopies to resolve the nature of the Mn ligands in our samples (19, 21). EPR spectra of intracellular Mn^{2+} qualitatively paralleled the elemental analysis (Fig. 1*B*), showing an over 10-fold greater accumulation of Mn in WT cells grown in the presence of 600 μM MnEDTA (Fig. 7*A*, *black line*) relative to cells grown with the standard 6 μM MnEDTA (*red line*). *vtc1-1* cells exhibited reduced capacity to accumulate Mn (~4-fold) compared with CC-4532 and *VTC1* complemented strain (Fig. S10). We therefore used the BODIPY-based fluorescent probe M1, specific for Mn^{2+} (57), to assess Mn accumulation in *vtc1-1* and the complemented strain. Fig. S11 shows that the M1 probe both 1) supported reduced Mn accumulation in the mutant and 2) showed localization within a lysosensor-positive organelle. Note that the sensitivity of the M1 probe is insufficient to detect Mn within acidocalcisomes of cells grown under normal Mn nutrition conditions.

Mn^{2+} in both genotypes showed the narrow EPR signal (small zero-field splitting) with a resolved six-line ^{55}Mn hyperfine pattern centered at g-2 (~12 kG) of Mn^{2+} coordinated in the high-symmetry, octahedral geometry commonly observed in Mn-metabolite complexes (Fig. S10). From the EXAFS results above, we hypothesized that Mn metabolites could be P-containing compounds (*e.g.* P_i, phytate (Phy), or polyPs, the last providing an elegant explanation for the loss of Mn accumulation in *vtc1-1* mutants, defective in polyP biogenesis). We therefore applied ENDOR/ESEEM spectroscopies to distin-

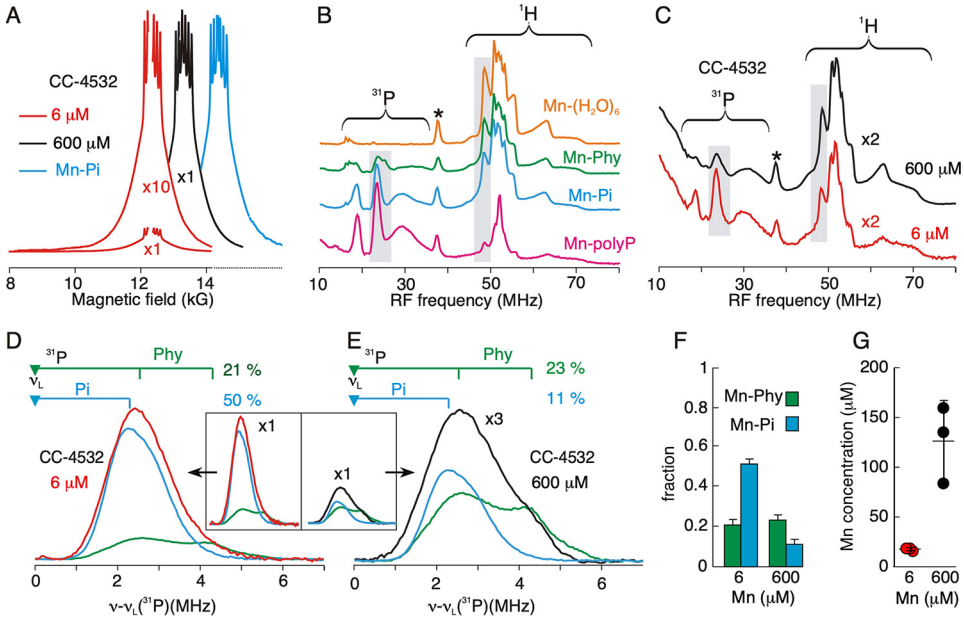

Figure 7. The final Mn "storage" ligand is not polyP in WT Chlamydomonas cells. EPR (*A*) and ENDOR (*B* and *C*) spectra were collected from WT cells (genotype CC-4532) grown in 6 or 600 μM MnEDTA. *x1* and *x10* represent magnification of EPR spectra. *B* presents ENDOR spectra for known Mn metabolite complexes as reference. The *braces* represent ENDOR responses of ^{31}P, ^{1}H nuclei. The ENDOR peaks in *gray highlights* are used to measure absolute ^{31}P and ^{1}H ENDOR responses, which are in turn used for calculating fractional contribution of different Mn metabolites to the cellular Mn ENDOR spectra. ENDOR spectra in *C* are magnified ×2. *, third harmonic peak of a ^{55}Mn ENDOR response at ~40 MHz (not shown). *D* and *E*, ^{31}P signals from WT cells grown in 6 μM (*D*) or 600 μM (*E*) MnEDTA. The ν_+ peaks of the ^{31}P ENDOR spectra shown here are centered around the ^{31}P Larmor frequency (ν_L) indicated by the *triangle* and shifted to higher frequency by half the hyperfine coupling, *A*/2 as indicated for Mn-Phy and Mn-P$_i$ metabolites. Note that the concentration of Mn^{2+} in all samples was adjusted to be equal to facilitate comparisons of peak heights for ^{1}H and ^{31}P features. *Inset*, original scale of spectra shown in *D* and *E*. *F* and *G*, fraction of Mn bound to Phy or P$_i$ in WT cells grown in normal- or excess-Mn conditions (*F*) and associated Mn concentrations (*G*); for *F*, the *error bars* are from the least-square fit of the ENDOR data. For *G*, the *horizontal bars* represent the mean for each sample ± S.D. (*error bars*) (n = 3). CW EPR conditions: MW frequency 34.8 GHz, T = 2 K, magnetic field scan rate 2 kG/min, modulation amplitude 1 G. Davies ENDOR conditions: magnetic field ~12.5 kG, $t\pi/2$ = 60 ns, τ = 400 ns, Trf = 160 μs, repetition time = 10 ms.

guish among these candidate metabolites by comparing spectra derived from cells grown in 6 or 600 μM MnEDTA with spectra generated from standard solutions of Mn-P$_i$, Mn-Phy, and Mn-polyP (shown in Fig. 7*B*). The ^{1}H signals represent protons from water molecules bound to Mn, their intensity decreasing as the H_2O ligands of $Mn^{2+}(H_2O)_6$ are replaced by metabolite ligands. For each P$_i$ molecule binding to Mn, one water molecule is displaced, whereas in Mn-polyP complexes, virtually all water molecules are displaced. The presence and abundance of P-based ligands can itself be inferred from the presence of their ^{31}P signals: in short, the Mn^{2+} acts as an "indicator" of the relative concentrations of competing ligands free within the cellular environment.

^{31}P ENDOR spectra from Mn^{2+} in general show a doublet centered around the ^{31}P Larmor frequency and separated by a hyperfine coupling, A_{Pi} ~4; the peaks at lower/higher frequency are labeled as ν_+/ν_- (Fig. S12). Although in many spectra of P$_i$ and polyP complexes, the lower-frequency (ν_-) peak is not well-resolved, the single ν_+ peak is sufficient to characterize the complex. Mn-P$_i$ and Mn-polyP complexes show similar ^{31}P couplings, but they exhibit different relative amplitudes of the ^{31}P and ^{1}H ENDOR responses, which together allow identification of the contribution from P$_i$/polyP (21). Phytate complexes exhibit two partially overlapping doublets with hyperfine coupling A_{phy} ~4, 8 MHz. (Fig. S12); again, the ν_+ peaks are sufficient to characterize the complex, and the relative amounts of P$_i$ and phytate complexes can be deduced by decomposing an observed cellular ^{31}P ENDOR spectrum into individual component contributions.

For Mn-replete cells grown in 6 μM MnEDTA, by combining ^{31}P, ^{1}H absolute ENDOR response (Fig. 7*C*) and comparing them with standards (Fig. 7*B*), we discovered that Mn-P$_i$ and Mn-Phy complexes accounted for ~50 and ~21%, respectively, of the total cellular Mn^{2+} pool, with minimal contribution from polyP (Fig. 7 (*C*, *D*, and *F*) and Fig. S13): for every 10 cellular Mn^{2+} ions, 5 will have bound P$_i$, and another 2 will be in a complex with Phy. This result was surprising to us, as we had hypothesized a polyP-based ligand in light of the *vtc1* mutant phenotype. ENDOR spectra from cells grown in 600 μM MnEDTA were likewise incompatible with a polyP ligand; in these cells, the ^{31}P peak decreased, whereas the ^{1}H peak was higher, suggesting that the Mn was not predominantly associated with polyP, as predicted (Fig. 7, *C*, *E*, and *F*). Indeed, the analysis suggested that on average only about 1 in 10 Mn atoms was bound to P$_i$, whereas the fraction associated with Phy remained constant, with roughly 2 of 10 Mn complexed to Phy for every 10 Mn (Fig. 7 (*E* and *F*) and Fig. S13).

Cells grown under excess-Mn conditions accumulate Mn to about 10-fold the levels of Mn^{2+} found in cells grown in Mn-replete conditions (Figs. 1*B* and 7*G*). As a result, although the fraction of Mn-P$_i$ decreases with increasing Mn accumulation (Fig. 7, *D–F*), ENDOR-derived speciation shows that the total cellular pool of Mn-P$_i$ complexes in fact doubles between Mn supply levels of 6 and 600 μM. The fraction of Mn that binds Phy

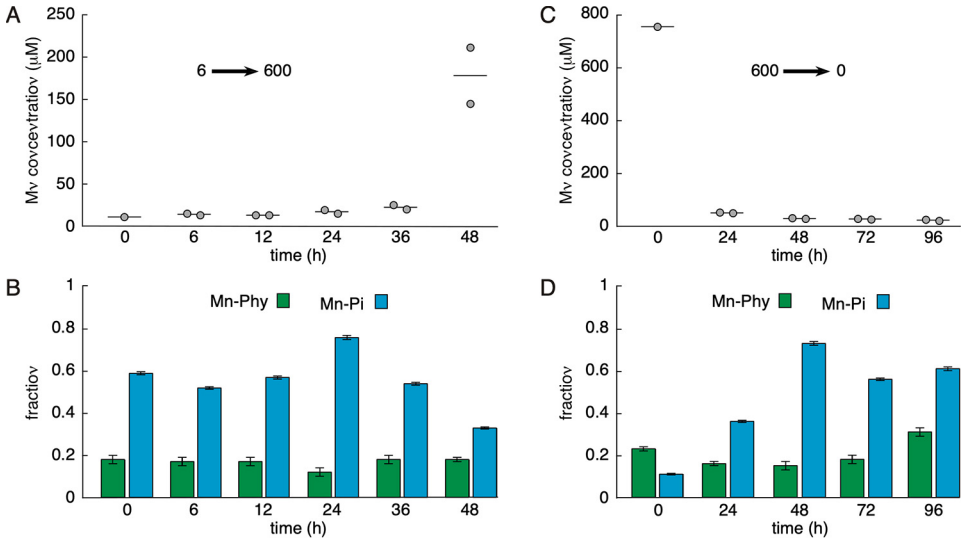

Figure 8. Time-course analysis of Mn ligand formation and disappearance. *A* and *B*, Chlamydomonas cells were first grown in 6 μM MnEDTA before being transferred to fresh medium supplied with 600 μM MnEDTA. Duplicate samples were collected over 48 h, and their Mn content was determined (A) as well as the fraction of Mn-metabolites bound to Phy or P_i (*B*). *C* and *D*, in the reciprocal experiment, cells were first grown in Mn-excess conditions in 600 μM MnEDTA before transfer to Mn-free medium. Again, Mn content (*C*) and the fraction of Mn-Phy and Mn-P_i (*D*) detected in samples over time were measured. The *error bars* in *B* and *D* are from the least-square fit of the ENDOR data.

does not change when cells are grown under excess Mn, so the total Mn-Phy cellular pool sees a 10-fold increase from 6 to 600 μM Mn. Thus, using Mn^{2+} as an indicator for its ligands and their concentrations, this means that as the cellular Mn^{2+} increases, so does the ratio of ligand concentrations, [Phy]/[P_i].

Despite higher absolute contributions from Mn-P_i and Mn-Phy, even under excess-Mn conditions, little Mn is bound by polyP. In addition, a careful investigation using ENDOR/ESEEM revealed no ^{14}N signals, which indicates that WT cells do not contain a significant population of Mn^{2+} coordinated by nitrogenous ligands. A high percentage of Mn may therefore be in a complex with ligand(s) not visible by ENDOR spectroscopy (most probably carboxylato metabolites).

Reversible sequestration of Mn by an ENDOR-silent ligand

The ENDOR results described above did not support the initial hypothesis that intracellular Mn^{2+} is bound to polyP. We wondered whether Mn^{2+} might, however, be transiently bound to polyP, which could be visualized in a time-course experiment. To this end, we first grew cells in 6 μM MnEDTA and then shifted them to fresh medium containing 600 μM MnEDTA to induce accumulation. We collected aliquots daily and measured intracellular Mn by elemental analysis and determined the fraction bound to Phy and P_i. Mn^{2+} accumulation only took place when cells reached the end of their exponential growth phase and transitioned to stationary (Fig. 8*A*). These results align well with the timing of polyP accumulation inside acidocacisomes in Chlamydomonas and other unicellular eukaryotes (58), again suggesting that polyP is an important contributor to Mn accumulation, even if we cannot detect substantial Mn-polyP metabolites. ENDOR spectroscopy of the same samples revealed constant Mn-Phy levels of about 20% and Mn-P_i levels around 60% before cells reached stationary phase. However, as cells began to accumulate 15 times the levels of Mn between 36 and 48 h after inoculation, Mn-P_i levels concomitantly decreased by 50%, with minimal contribution from Mn-polyP complexes (Fig. 8*B*), further arguing against a role for polyP as the Mn ligand at any stage during Mn accumulation (Fig. 8*B*).

In a reciprocal experiment, we transferred cells adapted to Mn excess into fresh medium with no added MnEDTA and collected samples every day. Cellular Mn content decreased drastically within 24 h and stabilized within 2 days, as cells first mobilized their intracellular stores to sustain growth (Fig. 8*C*). Mn-P_i levels mirrored the changes in intracellular Mn: the fraction of Mn-P_i complexes increased sharply within 2 days following the step down from 600 μM to 0 μM MnEDTA, but Mn-polyP complexes did not appear (Fig. 8*D*).

These results demonstrate that cells 1) accumulate Mn at the end of the exponential growth phase, 2) do not rely on polyP as a final storage form of Mn complexes, and 3) can quickly remobilize accumulated Mn during micronutrient scarcity, consistent with our earlier observation (Fig. 5).

Imidazole becomes a manganese ligand in the absence of polyP

What is the Mn^{2+} speciation in the *vtc1-1* mutant, which lacks polyP? ENDOR spectroscopy identified the Mn-P ligand complexes mainly as Mn-Phy (40%), with minimal contribution from Mn-P_i (Fig. 9, *A* and *B*). Surprisingly, in contrast to WT (CC-4533 and *VTC1* complemented strains), the *vtc1-1* mutant had a significant population of Mn-^{14}N metabolites when grown under Mn-replete conditions. As depicted in Fig. 9*C*, the Mn-imidazole complex shows a strong three-pulse ESEEM time-wave modulation, which is caused by Mn-^{14}N electron nuclear hyperfine coupling to a bound imidazole. Under identical assay conditions (namely, samples were set to have equal amounts of Mn during the assay), the *vtc1-1* mutant generated time-wave traces similar to those of the reference Mn-imidazole complex but with a signal amplitude only 20% of that from Mn-imidazole.

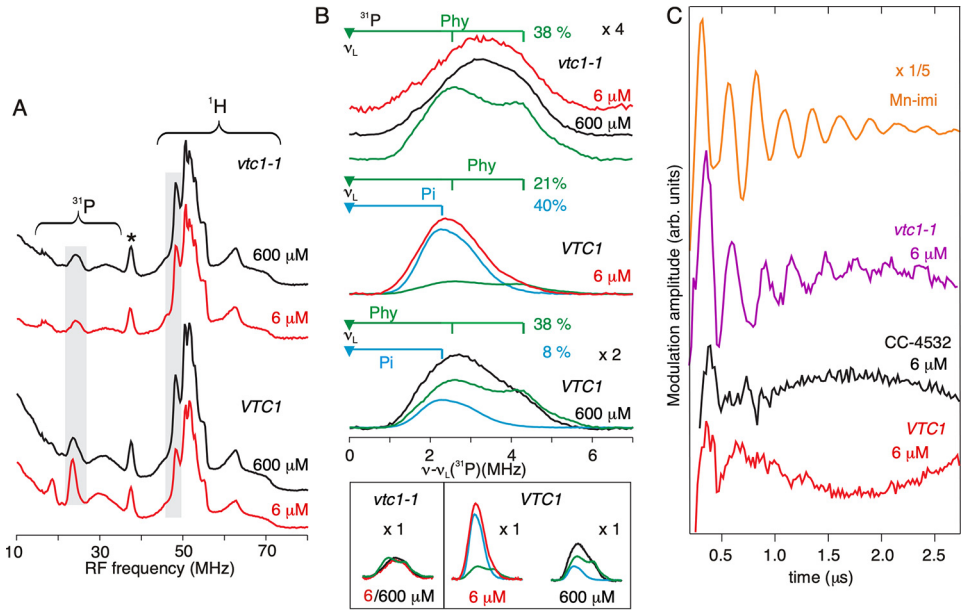

Figure 9. Imidazole compounds as opportunistic Mn ligand in *vtc1-1*. ENDOR (*A* and *B*) and ESEEM (*C*) spectra were collected from CC-4532, *VTC1*, and *vtc1-1* cells grown in 6 or 600 μM MnEDTA. Note that the concentration of Mn in all samples was adjusted to be equal and therefore facilitate comparisons of peak heights for ^{1}H and ^{31}P features. *A*, full ENDOR spectra for *vtc1-1* and *VTC1* cells grown in 6 and 600 μM MnEDTA. *B*, ^{31}P nu+ features from *vtc1-1* and *VTC1* cells grown in 6 or 600 μM Mn, with individual contributions from Mn-phytate and Mn-P$_i$ metabolites indicated *above* each set of spectra as in Fig. 7. *Bottom inset*, original scale of spectra shown in *B*. *C*, ESEEM spectra for Mn-imidazole (*Mn-Imi*), *VTC1*, and *vtc1-1* cells grown in 6 μM MnEDTA. The magnitude of ^{14}N time wave modulation of Mn-imidazole complex is multiplied by $^{1}/_{5}$ to match that from *vtc1-1*; both have the same Mn^{2+} concentration. ENDOR conditions: as in Fig. 7. ESEEM conditions: magnetic field ~12.5 kG, $t\pi/2 = 50$ ns, $\tau = 400$ ns, repetition time = 10 ms.

These results therefore indicate that ~20% of the cellular Mn^{2+} ions in *vtc1-1* are bound to an imidazole-type ligand in *vtc1-1*, presumably histidine-based, which could arise from low-molecular-weight metabolites and/or Mn-containing enzymes. In the green lineage, MnSODs and the oxygen-evolving complex are the main Mn-bound enzymes, but the EPR spectra show no contribution from either and allow us to rule both out as the source of the imidazole-based ligand in *vtc1* (59, 60). The two WT strains (CC-4532 and the *VTC1* complemented strain) have no discernable Mn-imidazole signal (Fig. 9*C*). Mn-imidazole metabolites may be present in WT strains, but their signal could be masked by Mn-P metabolites.

Discussion

To prevent mismetalation of enzymes that incorporate iron, zinc, or manganese as cofactors, cells maintain a limited cytosolic pool of these transition metals by the concerted action of regulated uptake and sequestration from the cytosol (17). In the unicellular alga *C. reinhardtii* and all photosynthetic organisms, mitochondrial superoxidase dismutases and the chloroplast photosystem II complex represent the main Mn sinks in the cell. Although Mn sequestration by the plant vacuole, Golgi, and endoplasmic reticulum have been established, how Chlamydomonas copes with and stores excess Mn is unclear. Our results, comprising observations from complementary approaches, implicate a lysosome-related organelle, the acidocalcisome, as the main sequestration site for cellular Mn.

NanoSIMS (Fig. 2), XFM (Fig. S3), and EDX spectroscopy (Fig. S4) demonstrated co-occurrence of Mn with Ca and P, both markers of acidocalcisomes (38, 48, 49, 61). A *vtc1* mutant defective in the function of the VTC complex was unable to accumulate Mn to WT levels under Mn-replete conditions (6 μM MnEDTA) and failed to accumulate Mn under excess conditions (600 μM MnEDTA) (Figs. 3 and 5). The VTC complex localizes to the vacuolar membrane and catalyzes the synthesis of polyP chains of variable length (from tens to hundreds of P$_i$ residues) by pulling P$_i$ from the cytosol and translocating the elongating polyP chain into the vacuole in an ATP-dependent manner. The polyP inside acidocalcisomes is likely to accumulate in a low-pH environment, surrounded by cations like Ca^{2+}, Mg^{2+}, and K^{+}, bringing polyP close to quantitative precipitation (49). Chlamydomonas *vtc1* mutants lack electron-dense regions (observed by TEM and TEM-EDX in WT cells; Fig. S4) due to the loss of polyP crystals, likely associated with Ca^{2+}. Nonetheless, we visualized intact acidocalcisomes in both WT and *vtc1* mutant cells with Lysosensor (Fig. 4), and their membrane appears functional based on their ability to maintain internal acidity from the concerted proton concentration gradient generated by the H^{+}-pyrophosphatase and V-ATPase, whose abundances are not changed in the *vtc1* mutant (Fig. 4 and Fig. S7).

Chlamydomonas cells do not accumulate Mn when their cellular P levels are lowered genetically (as in the *vtc1-1* mutant; Fig. 3) or nutritionally (Fig. S8). Mutations in the Vtc1 and Vtc4 subunits of the yeast VTC complex prevent accumulation of another divalent metal ion (Mg) inside the vacuole (37), suggesting that polyP is a general and critical component of metal sequestration. The underlying mechanism for Mg^{2+} uptake does not rely on a dedicated transporter at the plasma membrane, but instead calls upon endocytosis from the growth medium and concentration into the vacuole of a Mg-EDTA

complex, with later stripping of the chelator agent and formation of a Mg-polyP complex (37).

Unlike Mg^{2+}, which has no unpaired electrons and is hence invisible to paramagnetic resonance spectroscopies, the coordination state of Mn^{2+} can be probed using EPR/ENDOR/ESEEM spectroscopies (19, 21). Hypotheses concerning divalent cation accumulation (37) can therefore be tested with Mn^{2+}, but not for Mg^{2+}. EPR spectra from Mn-accumulating cells categorically demonstrate that cellular Mn is not found complexed to EDTA, as the observed EPR signals display only the relatively narrow signal of a high-symmetry metabolite complex with well-defined six-line ^{55}Mn hyperfine pattern, which is very distinct from the broad and low-symmetry signal of Mn-EDTA, with a negligible ^{55}Mn hyperfine pattern (62). EPR spectroscopy therefore argues against significant uptake of EDTA from the growth medium by Chlamydomonas cells, even in the presence of 1 mM EDTA.

Our results show that Mn^{2+} accumulates in the acidocalcisomes and further reveal that Mn^{2+} is found as mononuclear complexes with inorganic P_i and Phy, but not polyP. Further, EPR measurements of Mn^{2+} in the presence of polyP do not suggest that polyP can form antiferromagnetically coupled polynuclear polyP-Mn^{2+} complexes (Fig. S9), and the conclusion that virtually all of the Mn is in the Mn^{2+} state is supported by the parallelism of changes in total Mn and in EPR-detectable Mn^{2+}. Under replete conditions (6 μM MnEDTA), about 70% of total Mn^{2+} was complexed to either P_i or Phy, but the contribution from polyP complexes was minimal (Figs. 7 and 9 and Figs. S11 and S12). Under Mn excess conditions (600 μM MnEDTA), Mn-P_i levels doubled, whereas Mn-Phy levels increased 10 times; however, together, Mn-P_i and Mn-Phy only accounted for one-third of the total Mn accumulated in these cells, with the remaining two-thirds of the pool of Mn^{2+} likely coordinated to carboxylato metabolites, which are ENDOR-silent. Again, polyP had a minimal contribution to final Mn complexation. Nevertheless, polyP must be present in cells to permit translocation of Mn into acidocalcisomes, as Chlamydomonas *vtc1* mutants cannot accumulate Mn, pointing to a transitory role for polyP in Mn homeostasis.

The speciation profile of Mn in *vtc1* mutants was very distinct from WT cells: ENDOR features derived from ^{31}P markedly decreased in the *vtc1-1* mutant (Fig. 9, *A* and *B*), consistent with a much greater contribution from ENDOR-silent ligands. However, ESEEM spectroscopy shows that ~20% of Mn^{2+} takes on an imidazole-based metabolite as a ligand in the absence of polyP, possibly acting to concentrate this divalent transition metal into acidocalcisomes. A similar population of Mn^{2+}-imidazole complexes was observed previously in *D. radiodurans* (19).

We were surprised by how effective Chlamydomonas cells were at accumulating Mn, which is in stark contrast to the rates of uptake for Cu (41) and Fe (13), which becomes restricted once the cell has the amount it needs to maintain metalloprotein quotas. Much of the work on high Mn tolerance comes from yeast: a loss of function in the MnSOD enzyme Sod1p causes elevated oxidative stress, but this can be rescued by high concentrations of exogenous Mn. Once inside the cell, cytosolic Mn forms complexes with P_i and can then compensate for the loss of Sod1p due to its high intrinsic superoxide dismutase activity (20). Mn and P metabolism are largely co-dependent: Mn and P are thought to be co-transported by phosphate transporters, which is supported by the lower Mn content of phosphate transporter mutants (36, 63, 64). However, not all yeast mutants with altered P content agree with this model, unless their polyP pool is also taken into account. For example, *pho80* mutants exhibit a constitutive P deficiency phenotype, leading to 1) increased P uptake, 2) high polyP levels, and 3) much higher intracellular Mn content (34, 46). The Mn pool in *pho80* mutants is presumed to be cytosolic, but we hypothesize a vacuolar localization, where polyP acts as a molecular magnet to sequester Mn away from the cytosol, thereby robbing *pho80* cells from Mn-catalyzed detoxification protection. In agreement with our hypothesis, Chlamydomonas *vtc1* mutants and yeast *vtc* mutants fail to accumulate Mn and have much lower polyP levels (35, 36, 48, 50) and may offer an alternative and more comprehensive explanation that ties Mn and P metabolism via polyP.

The crystal structure of the catalytic domain of yeast Vtc4 exposes another factor potentially contributing to the high capacity of cells to accumulate Mn (52). The substrate-binding site is coordinated with Mn^{2+} via six positively charged and one negatively charged amino acids and a tyrosine residue that are conserved between yeast and Chlamydomonas (Fig. S14). Vtc4p is inactive without a metal cofactor, and Mn^{2+} cations offered the strongest stimulation of polyP synthesis, followed by Zn^{2+}, Co^{2+}, Mg^{2+}, and Ni^{2+} (52). The potential for accumulation may become obscured by the associated toxicity of the transition metal, as would be expected for Zn^{2+}, Co^{2+}, and Ni^{2+}. Only in the case of Mn^{2+} (this study) and Mg^{2+} (37) will the metals be taken up by cells and stored inside acidocalcisomes, all the more so that Mn^{2+} and Mg^{2+} will stimulate polyP synthesis in a feed-forward loop, as long as cytosolic inorganic P is available.

Previous attempts at estimating the Mn quota of healthy Chlamydomonas cells did not distinguish between Mn pools participating in photosynthesis or stored in acidocalcisomes. The pool of Mn sequestered inside the vacuole is fully bioavailable when cells are faced with Mn scarcity conditions (Fig. 5). The Chlamydomonas *vtc1* mutant cannot synthesize or store polyP in its acidocalcisomes and therefore lacks one major cellular Mn sink, which grants us access to the photosynthetic Mn quota, which we estimate to be $\sim 2 \times 10^7$ Mn atoms/cell (instead of the previous estimate of $4–5 \times 10^7$ Mn atoms per cell; Fig. 3) (65). Likewise, we can estimate the polyP content of Chlamydomonas cells relative to total P content using the *vtc1* mutant: about 60% of all cellular P is engaged in polyP and other low molecular weight complexes.

In conclusion, we show here that Chlamydomonas cells can accumulate the transition metal Mn^{2+} to very high levels, complexed in part with P_i and phytate metabolites. PolyP is critical for this process but is not the final ligand for Mn, as little Mn-polyP complex is found in any of the variants studies. Instead, we propose that Chlamydomonas cells utilize polyP to concentrate Mn^{2+} cations into acidocalcisomes. At least in yeast, high cytosolic levels of polyP are toxic, and polyP cannot be translo-

cated to the vacuole from the cytosol (66). The role of polyP in Mn^{2+} uptake is likely restricted to the acidocalcisomes, where we propose it plays an escorting role to a final and currently unknown ligand(s). Our results may also cast the role of polyP in Mg^{2+} acquisition in a different light (37). Our results offer the testable alternative that the final ligand for Mg^{2+} does not in fact contain phosphates, as initially presumed (37). The speciation state of Mn^{2+} will provide an excellent indicator for the yeast vacuolar environment in cells grown in the presence of high concentrations of EDTA. The ability to identify whether EDTA is an intracellular ligand will shed light on the sequestration of metals into acidocalcisomes/vacuoles in Chlamydomonas and yeast and will refine the role of polyP within this cellular context.

Experimental procedures

Strains and culture conditions

C. reinhardtii WT strain CC-4532, mutant strain *vtc1-1* (CC-5321), and *vtc1-1* strain complemented with the *VTC1* locus (here referred to as *VTC1, CC-5324*) were cultured in Tris acetate-phosphate (TAP) medium with revised trace elements (65). Cultures were incubated at 24 °C with constant agitation (180 rpm) in an Innova incubator (New Brunswick Scientific, Edison, NJ) in continuous light (~100 μmol of photons per $m^{-2}{\cdot}s^{-1}$) provided by cool white fluorescent bulbs (4100 K) and warm white fluorescent bulbs (3000 K) in a ratio of 2:1. High photon flux density (350–420 μmol of photons per $m^{-2}{\cdot}s^{-1}$) was provided by a white fluorescent bulb (3800 K).

Where indicated, excess manganese was supplied as EDTA-chelated $MnCl_2$. Manganese-deficient medium was prepared without Mn supplementation (5). For photoautotrophic growth, acetate was eliminated from TAP medium, the pH was adjusted to 7.4 with HCl, and the cultures were bubbled with air. Phosphorus-free medium (Tris acetate, TA), was prepared by replacing potassium phosphate with 1.2 mM potassium chloride (67).

For all treatments, precultures were grown in TAP medium until mid-log growth phase (3–5 $\times$ 10^6 cells/ml) and then used to inoculate test cultures at an initial cell density of 1 $\times$ 10^4 cells/ml. Cultures were collected for analysis at a density of 3–4 $\times$ 10^6 cells/ml. For phosphorus deficiency, cells grown in TAP medium were collected by centrifugation (3,500 $\times$ *g*, 3 min) and washed twice with TA medium prior to inoculation in TA medium containing the indicated amounts of manganese at cell density of 1 $\times$ 10^5 cells/ml (67).

The *vtc1-1* mutant and complemented strain (*VTC1*) were grown in photoautotrophic conditions for 2 rounds (1 week each) with 6 μM Mn with air bubbling. For pretreatment, flasks were inoculated at 1 $\times$ 10^4 cells/ml with 6 or 600 μM Mn and allowed to grow for 1 week with air bubbling. Cells were collected by centrifugation for 5 min at room temperature and washed twice in 5 mM EDTA and once in milliQ water. Test flasks with no added Mn were inoculated with washed cells at a density of 5 $\times$ 10^4 cells/ml and grown for 7 days with air bubbling.

For cell size analysis, a Cellometer Auto M10 (Nexcelom Bioscience) was used. Samples from three independent experiments were collected at mid-log growth phase, and cell diameter was determined from 1,100 cells/sample.

Chlorophyll content and chlorophyll fluorescence measurements

Chlorophyll was extracted from whole cells with an acetone/methanol (80:20, v/v) mixture. Total chlorophyll (*a* and *b*) content was estimated from the absorbance at 646.6 and 663.6 nm measured on a PerkinElmer Life Sciences LAMBDA 25 UV-visible spectrometer with absorbance at 750 nm as a reference to remove background from cell debris, as described (68). Each measurement was done in two technical replicates collected from three independent experimental replicates.

Minimum chlorophyll fluorescence (F_o) and maximum quantum yield of photosystem II (F_v/F_m) were determined in cells after 10-min dark adaptation under a saturating pulse with an IMAGING-PAM MAXI chlorophyll fluorometer and ImagingWin software (Heinz Walz, Effeltrich, Germany).

Elemental content measurements

1 $\times$ 10^8 cells from all cultures were collected by centrifugation at 3,500 $\times$ *g* for 3 min and washed three times with 1 mM Na_2-EDTA, pH 8.0, to remove metals associated with the cell surface and twice with Milli-Q water. After removing the remaining water by brief centrifugation, cell pellets were digested with 70% nitric acid at room temperature overnight and at 65 °C for 2 h. Digested samples were diluted with Milli-Q water to a final nitric acid concentration of 2% (v/v). To measure metal content of culture medium, aliquots of the medium were treated with nitric acid and diluted with Milli-Q water to reach a final concentration of 2% nitric acid (v/v). Elemental analysis was measured by inductively coupled plasma MS on an Agilent 8800 Triple Quadrupole ICP-MS instrument using three standards for calibration (an environmental calibration standard (Agilent 5183–4688), phosphorus standard (Inorganic Ventures CGP1), and sulfur standard (Inorganic Ventures CGS1)) and two internal standards (^{89}Y and ^{45}Sc (Inorganic Ventures MSY-100PPM and MSSC-100PPM, respectively)). Elements were determined in MS/MS mode and measured in a collision reaction cell using helium for the measurement of ^{55}Mn, ^{63}Cu, and ^{66}Zn; hydrogen for ^{56}Fe and ^{40}Ca; and oxygen for ^{31}P as gas, as described previously (69). Each sample was measured in four technical replicates, and variation between technical replicates did not exceed 5%.

Nanoscale secondary ion MS

3 $\times$ 10^6 cells from WT laboratory strain CC-4532 from three independent cultures were collected by centrifugation (3,500 $\times$ *g*, 5 min) and washed twice with 10 mM sodium phosphate, pH 7.0, before immersion in a fixing solution containing 2% glutaraldehyde and 2% paraformaldehyde in 0.1 M sodium phosphate, pH 7.4, for 2 h at room temperature and then incubated at 4 °C.

Cells were washed five times with 0.1 M sodium phosphate buffer, pH 7.4, and post-fixed in a solution of 1% OsO_4 in sodium phosphate buffer, pH 7.4. Samples were further washed four times in Na acetate buffer, pH 5.5, and dehydrated in an ethanol gradient (50, 75, 95, 100, 100, and 100%) for 10 min each. Dehydrated samples were passed through propylene

oxide and infiltrated in a 1:1 mixture of Epon 812 and propylene oxide for 2 h and in a 2:1 mixture for 2 h. Finally, the previous mixture was infiltrated in pure Epon 812 overnight and cured in an oven at 60 °C for 48 h. Sections of 200-nm thickness (gray interference color) were cut on an ultramicrotome (RMC MTX) using a diamond knife and deposited on 100-mesh carbon-coated molybdenum grids (G100-Mo, Electron Microscopy Sciences).

For nanoSIMS imaging of the intracellular distribution of bound P, Ca, and Mn, we used the LLNL CAMECA NanoSIMS 50 (Gennevilliers, France) (70–72). Sectioned cells were first located and imaged by a JEOL 7401 field emission electron microscope in scanning transmission EM (STEM) mode. Then they were relocated and analyzed in the NanoSIMS 50. A focused negative oxygen ion primary beam was scanned over the sample to generate secondary ion images. The secondary ion mass spectrometer was tuned for ~3,500 mass resolving power ($M/\Delta M$, 1.5× correction) (73), and $^{12}C^+$, $^{31}P^+$, $^{40}Ca^+$, and $^{55}Mn^+$ were detected simultaneously by electron multipliers in pulse counting mode. The correct metal ion peaks were identified using NBS610 glass (National Institute of Standards and Technology). The analysis areas were first sputtered with high current (~1.2 nA O^-, 55 × 55 μm^2, 256 × 256 pixels, 1 ms/pixel, 11 cycles, depth ~30 nm) (70) to establish sputtering equilibrium, followed by moderate spatial resolution analysis (~500 nm, 200 pA O^-, 50 × 50 μm^2, 256 × 256 pixels, 1 ms/pixel, 50 cycles). Higher spatial resolution images were also collected (~200 nm, 30 pA, 50 × 50 μm^2, 512 × 512 pixels, 1 ms/pixel, 50 cycles).

The nanoSIMS ion image data were processed quantitatively using custom software (L'Image, L. R. Nittler, Carnegie Institution for Science, Washington, D. C.). The ion images were corrected for detector dead time and image shifts between scans and then used to produce ion images. Regions of interest (ROIs) were defined using an automated algorithm to subdivide the analyzed area into hexagons (Fig. S4). Hexagons that were not on cells were deleted. Ion ratios ($^{31}P^+/^{12}C^+$, $^{40}Ca^+/^{12}C^+$, and $^{55}Mn^+/^{12}C^+$) for each ROI were calculated by averaging the ratios over replicate scans. These data provide relative quantitative composition, but they were not standardized to provide concentration data.

Confocal microscopy

Chlamydomonas cells were cultured to early stationary phase and collected by centrifugation (3,500 × *g*, 3 min) and washed twice with 10 mM sodium phosphate, pH 7.5. All fluorescent dyes were diluted in 10 mM sodium phosphate, pH 7.5, to a final concentration of 2 μM. Cells were treated with a Lysosensor DND189, Lysosensor DND167, or M1 Mn probe and mounted on glass slides for immediate visualization. Cells treated with DAPI were first fixed for 10 min with 2% glutaraldehyde, followed by permeabilization with 40 μM digitonin for 10 min before mounting on glass slides for visualization. Microscopy was performed on a Zeiss LSCM Airyscan 880 (Fig. 6 (*C* and *D*) and Fig. S6) equipped with a ×63/1.4 oil immersion objective or a Zeiss Elyra using Lattice SIM with a ×100/1.46 oil objective (Fig. 6, *A* and *B*). Images were recorded using filter sets or spectral mode as indicated in the figure legends. All aspects of image capture were controlled via Zeiss ZEN Black software, including fluorescent emission signals from probes and/or chlorophyll.

X-ray absorption spectroscopy

Multiple independent samples of 5 × 10^8 cells from cultures treated with excess manganese were collected by centrifugation (3,500 × *g*, 5 min) and washed twice with 1 mM EDTA and twice with Milli-Q water to remove metals associated with the cell surface and subsequently washed with 10 mM sodium phosphate. After removing the liquid, cells were suspended in 30% glycerol (v/v) (estimated from volume of cell pellet) and loaded with a Hamilton syringe into a Kapton-wrapped lucite XAS sample cell and flash-frozen in liquid nitrogen. Samples were stored in liquid nitrogen until beam exposure. XAS data were collected at the Stanford Synchotron Radiation Lightsource on beamline 9-3, which is equipped with a Si(220) double-crystal monochromator, equipped with a focusing mirror that also provides harmonic rejection. Fluorescence spectra were collected using a 100-element germanium solid-state detector from Canberra. During data collection, the Oxford Instruments continuous-flow liquid helium cryostat was stabilized at 10 K. Manganese data were collected using a 3-μm chromium filter placed between the cryostat and the detector to reduce unassociated scattering. Mn foil spectra were collected simultaneously with the protein data for energy calibration. The first inflection point for Mn was set at 6,543.3 eV. Manganese XAS spectra were recorded using 5-eV steps in the pre-edge regions and 0.25-eV steps in the edge regions and 0.05 $Å^{-1}$ increments in the EXAFS region (to $k = 13$ $Å^{-1}$), integrating from 1 to 20 s in a k^3-weighted manner. An average of 6 scans were collected and averaged for each sample. Each scan lasted ~45 min. Each spectrum was closely monitored for X-ray–induced radiation damage.

XAS spectra were processed and analyzed using the EXAFSPAK program suite written for Macintosh OSX. Fluorescence scans corresponding to each channel were examined for anomalies. A Gaussian function was used in the pre-edge region, and a three-region cubic spline was used in the EXAFS region. EXAFS data were converted to *k* space using E_0 values of 6,560.00 eV. Spectra were simulated using single and multiple scattering amplitude and phase functions generated using the Feff version 8 software package integrated within EXAFSPAK. Single scattering models were calculated for oxygen, nitrogen, phosphorous, and carbon to simulate possible manganese ligand environments. Calibrated scale factors (Sc) and model E_0 values were not allowed to vary during fitting; the Sc for manganese samples was 0.95. Mn data were fit out to a *k* value of 13.0 $Å^{-1}$. Calibration from Mn (II) and Mn(III) theoretical model compounds were used to determine the fit E_0 and Sc parameters. E_0 values for Mn-O, Mn-C were set at −10, and Mn-P was set at −12. EXAFS spectra were simulated using both filtered and unfiltered data; however, simulation results were presented for only fits to raw (unfiltered) data. Simulation protocols and criteria for determining the best fit were as described previously (56).

Electron paramagnetic and electron nuclear double resonance

2×10^8 cells from cultures were collected by centrifugation (3,500 × *g*, 5 min), and metals associated with the cell surface were removed by washing twice with 1 mM EDTA, pH 8, and twice with Milli-Q water. After a subsequent wash with 50 mM HEPES, pH 7.0, cells were resuspended in 30% glycerol in 50 mM HEPES, pH 7.0, and loaded into an ENDOR sample tube, flash-frozen in liquid nitrogen, and stored at −80 °C until analysis (21). 35-GHz CW EPR spectra were recorded using a laboratory-built 35-GHz EPR spectrometer (74). As described previously (21), the absorption-display EPR spectra (collected from cellular Chlamydomonas and Mn-metabolites by using continuous-wave (CW) "rapid passage" methods at 2 K) are characteristic of an $S = 5/2$ ion with small zero-field splitting (ZFS), with the principal ZFS parameter, D, much less than the microwave quantum ($h\nu$). Such spectra show a central 55Mn ($I = 5/2$) sextet arising from hyperfine interactions, $A \sim 91$ G, that is associated with transitions between the $m_s = +1/2$ and $-1/2$ electron-spin substrates. These features "ride on" and are flanked by significantly broader signals from the four "satellite" transitions involving the other electron-spin substrates ($m_s \pm 5/2 \leftrightarrow \pm 3/2$; $\pm 3/2 \leftrightarrow \pm 1/2$). The net absorption spectrum is the sum of the five envelopes of these five transitions among substrates.

Pulsed ENDOR/ESEEM spectra were recorded using a laboratory-built 35-GHz pulsed EPR spectrometer (75). All spectra were recorded at 2 K, which was achieved using an immersion helium cryostat. ^{31}P, ^{1}H Davies ENDOR spectra were recorded using the pulse sequence (π-T-π/2-τ-π-τ-echo), where T is the time interval for which the radiofrequency pulse is randomly hopped. ENDOR of a paramagnetic metal ion center, such as Mn^{2+}, provides an NMR spectrum of the nuclei that is hyperfine-coupled to the electron spin (76) and thus can be used to identify and characterize coordinating ligands (77, 78). The frozen-solution spectrum of an $I = 1/2$ nucleus, such as ^{31}P and ^{1}H, coupled to Mn^{2+} comprises a set of doublet features centered at the nuclear Larmor frequency and split by multiples of the electron-nuclear hyperfine coupling (A). The primary doublet is associated with the $m_s = \pm 1/2$ electron spin sublevels of Mn^{2+} and is split by A; weaker satellite doublets associated with the $m_s = \pm 3/2$ and $\pm 5/2$ sublevels are split by 3A and 5A. All spectra in this study display ^{1}H signals that can be assigned to the protons of bound water. In addition, all of the spectra, except for the aqueous solution, show a sharp $m_s = \pm 1/2$ ^{31}P doublet from a phosphate moiety bound to the Mn^{2+} center. The intensities of ^{31}P and ^{1}H signals differ significantly among the spectra, and analysis of these intensities provides a means of assessing cellular Mn^{2+} speciation (21).

Three-pulse ESEEM spectra were recorded using the pulse sequence, $\pi/2 - \tau - \pi/2 - T - \pi/2 - \tau -$ echo, where T is the time varied between second and third microwave pulses, with four-step phase cycling to suppress unwanted Hahn and refocused echoes (79). A ^{14}N nucleus ($I = 1$) directly coordinated with ^{55}Mn creates modulation in the electron spin echo decay, which is dominated by ^{14}N hyperfine interaction. To quantitate ^{14}N ESEEM responses from cellular Mn^{2+}, we chose as a standard the ^{14}N response from the Mn-imidazole complex, which binds one imidazole and (presumably) five waters.

Author contributions—M. T., M. C., P. A. S., A. S., B. E. L., S. R. S., D. S., K. H., M. S. O., S. C., C. R., M. R., P. K. W., T. L. S., J. P.-R., B. M. H., and S. S. M. data curation; M. T., M. C., P. A. S., A. S., B. E. L., S. R. S., D. S., K. H., M. S. O., S. C., C. R., M. R., P. K. W., T. L. S., J. P.-R., and S. S. M. formal analysis; M. T., A. S., B. E. L., S. R. S., D. S., K. H., M. S. O., S. C., C. R., M. R., P. K. W., T. L. S., J. P.-R., B. M. H., and S. S. M. investigation; M. T., A. S., B. E. L., S. R. S., K. H., M. S. O., S. C., C. R., M. R., P. K. W., T. L. S., J. P.-R., B. M. H., and S. S. M. methodology; M. C. and S. S. M. supervision; M. C., A. S., B. E. L., S. R. S., K. H., M. S. O., S. C., C. R., and M. R. visualization; M. C. and P. A. S. writing-original draft; M. C., M. S. O., M. R., P. K. W., T. L. S., J. P.-R., B. M. H., and S. S. M. project administration; P. A. S. and S. S. M. writing-review and editing; K. H. validation; M. S. O., M. R., P. K. W., T. L. S., J. P.-R., B. M. H., and S. S. M. funding acquisition; K. K., S. D., A. D., M. R., and B. M. H. resources; B. M. H. and S. S. M. conceptualization.

Acknowledgments—We acknowledge use of the Advanced Photon Source, a United States Department of Energy (DOE) Office of Science User Facility operated for the DOE Office of Science by Argonne National Laboratory under Contract DE-AC02-06CH11357. We thank Janice Pennington and Julio Paez Valencia for help handling samples and with the EDX analysis. Portions of this research were carried out at the Stanford Synchrotron Radiation Lightsource (SSRL). SSRL is a national user facility operated by Stanford University on behalf of the United States DOE, Office of Basic Energy Sciences. The SSRL Structural Molecular Biology Program is supported by the DOE, Office of Biological and Environmental Research, and by the National Institutes of Health, National Center for Research Resources, Biomedical Technology Program. Work at Lawrence Livermore National Laboratory was performed under the auspices of DOE Contract DE-AC52-07NA27344. Part of the research was performed at EMSL (Ringgold ID 130367), a DOE Office of Science User Facility sponsored by the Office of Biological and Environmental Research.

References

1. Kai, Y., Matsumura, H., and Izui, K. (2003) Phosphoenolpyruvate carboxylase: three-dimensional structure and molecular mechanisms. *Arch. Biochem. Biophys.* **414,** 170–179 CrossRef Medline
2. Requena, L., and Bornemann, S. (1999) Barley (*Hordeum vulgare*) oxalate oxidase is a manganese-containing enzyme. *Biochem. J.* **343,** 185–190 CrossRef Medline
3. Marschner, P. (2011) *Marschner's Mineral Nutrition of Higher Plants*, 3rd edition, Academic Press, Amsterdam
4. Page, M. D., Allen, M. D., Kropat, J., Urzica, E. I., Karpowicz, S. J., Hsieh, S. I., Loo, J. A., and Merchant, S. S. (2012) Fe sparing and Fe recycling contribute to increased superoxide dismutase capacity in iron-starved *Chlamydomonas reinhardtii*. *Plant Cell* **24,** 2649–2665 CrossRef Medline
5. Allen, M. D., Kropat, J., Tottey, S., Del Campo, J. A., and Merchant, S. S. (2007) Manganese deficiency in chlamydomonas results in loss of photosystem II and MnSOD function, sensitivity to peroxides, and secondary phosphorus and iron deficiency. *Plant Physiol.* **143,** 263–277 CrossRef Medline
6. Kliebenstein, D. J., Monde, R. A., and Last, R. L. (1998) Superoxide dismutase in *Arabidopsis*: an eclectic enzyme family with disparate regulation and protein localization. *Plant Physiol.* **118,** 637–650 CrossRef Medline
7. Vinyard, D. J., and Brudvig, G. W. (2017) Progress toward a molecular mechanism of water oxidation in photosystem II. *Annu. Rev. Phys. Chem.* **68,** 101–116 CrossRef Medline
8. Anbar, A. D. (2008) Oceans: elements and evolution. *Science* **322,** 1481–1483 CrossRef Medline

9. Fernando, D. R., Mizuno, T., Woodrow, I. E., Baker, A. J. M., and Collins, R. N. (2010) Characterization of foliar manganese (Mn) in Mn (hyper)accumulators using X-ray absorption spectroscopy. *New Phytol.* **188,** 1014–1027 CrossRef Medline
10. Spiller, S. C., Castelfranco, A. M., and Castelfranco, P. A. (1982) Effects of iron and oxygen on chlorophyll biosynthesis: I. *In vivo* observations on iron and oxygen-deficient plants. *Plant Physiol.* **69,** 107–10711 CrossRef Medline
11. Tottey, S., Block, M. A., Allen, M., Westergren, T., Albrieux, C., Scheller, H. V., Merchant, S., and Jensen, P. E. (2003) *Arabidopsis* CHL27, located in both envelope and thylakoid membranes, is required for the synthesis of protochlorophyllide. *Proc. Natl. Acad. Sci. U.S.A.* **100,** 16119–16124 CrossRef Medline
12. Moseley, J. L., Allinger, T., Herzog, S., Hoerth, P., Wehinger, E., Merchant, S., and Hippler, M. (2002) Adaptation to Fe-deficiency requires remodeling of the photosynthetic apparatus. *EMBO J.* **21,** 6709–6720 CrossRef Medline
13. Terauchi, A. M., Peers, G., Kobayashi, M. C., Niyogi, K. K., and Merchant, S. S. (2010) Trophic status of *Chlamydomonas reinhardtii* influences the impact of iron deficiency on photosynthesis. *Photosynth. Res.* **105,** 39–49 CrossRef Medline
14. Naumann, B., Busch, A., Allmer, J., Ostendorf, E., Zeller, M., Kirchhoff, H., and Hippler, M. (2007) Comparative quantitative proteomics to investigate the remodeling of bioenergetic pathways under iron deficiency in *Chlamydomonas reinhardtii*. *Proteomics* **7,** 3964–3979 CrossRef Medline
15. Höhner, R., Barth, J., Magneschi, L., Jaeger, D., Niehues, A., Bald, T., Grossman, A., Fufezan, C., and Hippler, M. (2013) The metabolic status drives acclimation of iron deficiency responses in *Chlamydomonas reinhardtii* as revealed by proteomics based hierarchical clustering and reverse genetics. *Mol. Cell Proteomics* **12,** 2774–2790 CrossRef Medline
16. Socha, A. L., and Guerinot, M. L. (2014) Mn-euvering manganese: the role of transporter gene family members in manganese uptake and mobilization in plants. *Front. Plant Sci.* **5,** 106 Medline
17. Imlay, J. A. (2014) The mismetallation of enzymes during oxidative stress. *J. Biol. Chem.* **289,** 28121–28128 CrossRef Medline
18. Long, J. C., and Merchant, S. S. (2008) Photo-oxidative stress impacts the expression of genes encoding iron metabolism components in chlamydomonas. *Photochem. Photobiol.* **84,** 1395–1403 CrossRef Medline
19. Sharma, A., Gaidamakova, E. K., Matrosova, V. Y., Bennett, B., Daly, M. J., and Hoffman, B. M. (2013) Responses of Mn^{2+} speciation in *Deinococcus radiodurans* and *Escherichia coli* to γ-radiation by advanced paramagnetic resonance methods. *Proc. Natl. Acad. Sci. U.S.A.* **110,** 5945–5950 CrossRef Medline
20. Barnese, K., Gralla, E. B., Cabelli, D. E., and Valentine, J. S. (2008) Manganous phosphate acts as a superoxide dismutase. *J. Am. Chem. Soc.* **130,** 4604–4606 CrossRef Medline
21. McNaughton, R. L., Reddi, A. R., Clement, M. H. S., Sharma, A., Barnese, K., Rosenfeld, L., Gralla, E. B., Valentine, J. S., Culotta, V. C., and Hoffman, B. M. (2010) Probing *in vivo* Mn^{2+} speciation and oxidative stress resistance in yeast cells with electron-nuclear double resonance spectroscopy. *Proc. Natl. Acad. Sci. U.S.A.* **107,** 15335–15339 CrossRef Medline
22. Lanquar, V., Ramos, M. S., Lelièvre, F., Barbier-Brygoo, H., Krieger-Liszkay, A., Krämer, U., and Thomine, S. (2010) Export of vacuolar manganese by AtNRAMP3 and AtNRAMP4 is required for optimal photosynthesis and growth under manganese deficiency. *Plant Physiol.* **152,** 1986–1999 CrossRef Medline
23. Eroglu, S., Giehl, R. F. H., Meier, B., Takahashi, M., Terada, Y., Ignatyev, K., Andresen, E., Küpper, H., Peiter, E., and von Wirén, N. (2017) Metal tolerance protein 8 mediates manganese homeostasis and iron reallocation during seed development and germination. *Plant Physiol.* **174,** 1633–1647 CrossRef Medline
24. Peiter, E., Montanini, B., Gobert, A., Pedas, P., Husted, S., Maathuis, F. J. M., Blaudez, D., Chalot, M., and Sanders, D. (2007) A secretory pathway-localized cation diffusion facilitator confers plant manganese tolerance. *Proc. Natl. Acad. Sci. U.S.A.* **104,** 8532–8537 CrossRef Medline
25. Eroglu, S., Meier, B., von Wirén, N., and Peiter, E. (2016) The vacuolar manganese transporter mtp8 determines tolerance to iron deficiency-induced chlorosis in *Arabidopsis*. *Plant Physiol.* **170,** 1030–1045 CrossRef Medline
26. Kim, S. A., Punshon, T., Lanzirotti, A., Li, L., Alonso, J. M., Ecker, J. R., Kaplan, J., and Guerinot, M. L. (2006) Localization of iron in *Arabidopsis* seed requires the vacuolar membrane transporter VIT1. *Science* **314,** 1295–1298 CrossRef Medline
27. Cailliatte, R., Schikora, A., Briat, J. F., Mari, S., and Curie, C. (2010) High-affinity manganese uptake by the metal transporter nramp1 is essential for *Arabidopsis* growth in low manganese conditions. *Plant Cell* **22,** 904–917 CrossRef Medline
28. Somers, I. I., and Shive, J. W. (1942) The iron-manganese relation in plant metabolism. *Plant Physiol.* **17,** 582–602 CrossRef Medline
29. Tanaka, A., and Navasero, S. A. (1966) Interaction between iron and manganese in the rice plant. *Soil Sci. Plant Nutr.* **12,** 29–33 CrossRef
30. Curie, C., Alonso, J. M., Le Jean, M., Ecker, J. R., and Briat, J.-F. (2000) Involvement of NRAMP1 from *Arabidopsis thaliana* in iron transport. *Biochem. J.* **347,** 749–755 CrossRef Medline
31. Thomine, S., Wang, R., Ward, J. M., Crawford, N. M., and Schroeder, J. I. (2000) Cadmium and iron transport by members of a plant metal transporter family in *Arabidopsis* with homology to Nramp genes. *Proc. Natl. Acad. Sci. U.S.A.* **97,** 4991–4996 CrossRef Medline
32. Milner, M. J., Seamon, J., Craft, E., and Kochian, L. V. (2013) Transport properties of members of the ZIP family in plants and their role in Zn and Mn homeostasis. *J. Exp. Bot.* **64,** 369–381 CrossRef Medline
33. Castaings, L., Caquot, A., Loubet, S., and Curie, C. (2016) The high-affinity metal transporters NRAMP1 and IRT1 team up to take up iron under sufficient metal provision. *Sci. Rep.* **6,** 37222 CrossRef Medline
34. Hürlimann, H. C., Stadler-Waibel, M., Werner, T. P., and Freimoser, F. M. (2007) Pho91 is a vacuolar phosphate transporter that regulates phosphate and polyphosphate metabolism in *Saccharomyces cerevisiae*. *Mol. Biol. Cell* **18,** 4438–4445 CrossRef Medline
35. Desfougères, Y., Gerasimaitė, R., Jessen, H. J., and Mayer, A. (2016) Vtc5, a novel subunit of the vacuolar transporter chaperone complex, regulates polyphosphate synthesis and phosphate homeostasis in yeast. *J. Biol. Chem.* **291,** 22262–22275 CrossRef Medline
36. Jensen, L. T., Ajua-Alemanji, M., and Culotta, V. C. (2003) The *Saccharomyces cerevisiae* high affinity phosphate transporter encoded by PHO84 also functions in manganese homeostasis. *J. Biol. Chem.* 278, 42036–42040
37. Klompmaker, S. H., Kohl, K., Fasel, N., and Mayer, A. (2017) Magnesium uptake by connecting fluid-phase endocytosis to an intracellular inorganic cation filter. *Nat. Commun.* **8,** 1879 CrossRef Medline
38. Docampo, R., and Huang, G. (2016) Acidocalcisomes of eukaryotes. *Curr. Opin. Cell Biol.* **41,** 66–72 CrossRef Medline
39. Lander, N., Cordeiro, C., Huang, G., and Docampo, R. (2016) Inorganic polyphosphate (polyP) physiology: polyphosphate and acidocalcisomes. *Biochem. Soc. Trans.* **44,** 1–6 CrossRef Medline
40. Blaby-Haas, C. E., and Merchant, S. S. (2014) Lysosome-related organelles as mediators of metal homeostasis. *J. Biol. Chem.* **289,** 28129–28136 CrossRef Medline
41. Hong-Hermesdorf, A., Miethke, M., Gallaher, S. D., Kropat, J., Dodani, S. C., Chan, J., Barupala, D., Domaille, D. W., Shirasaki, D. I., Loo, J. A., Weber, P. K., Pett-Ridge, J., Stemmler, T. L., Chang, C. J., and Merchant, S. S. (2014) Subcellular metal imaging identifies dynamic sites of Cu accumulation in *Chlamydomonas*. *Nat. Chem. Biol.* **10,** 1034–1042 CrossRef Medline
42. Daly, M. J., Gaidamakova, E. K., Matrosova, V. Y., Vasilenko, A., Zhai, M., Venkateswaran. A., Hess, M., Omelchenko, M. V., Kostandarithes, H. M., Makarova, K. S., Wackett, L. P., Fredrickson, J. K., and Ghosal, D. (2004). Accumulation of Mn(II) in Deinococcus radiodurans Facilitates Gamma-Radiation Resistance. *Science* **306,** 1025–1028 CrossRef Medline
43. Kropat, J., Gallaher, S. D., Urzica, E. I., Nakamoto, S. S., Strenkert, D., Tottey, S., Mason, A. Z., and Merchant, S. S. (2015) Copper economy in *Chlamydomonas*: prioritized allocation and reallocation of copper to respiration *vs*. Photosynthesis. *Proc. Natl. Acad. Sci. U.S.A.* **112,** 2644–2651 CrossRef Medline
44. Alejandro, S., Cailliatte, R., Alcon, C., Dirick, L., Domergue, F., Correia, D., Castaings, L., Briat, J. F., Mari, S., and Curie, C. (2017) Intracellular distri-

bution of manganese by the *trans*-Golgi network transporter NRAMP2 is critical for photosynthesis and cellular redox homeostasis. *Plant Cell* **29,** 3068–3084 CrossRef Medline

45. Andreeva, N., Ryazanova, L., Dmitriev, V., Kulakovskaya, T., and Kulaev, I. (2013) Adaptation of *Saccharomyces cerevisiae* to toxic manganese concentration triggers changes in inorganic polyphosphates. *FEMS Yeast Res.* **13,** 463–470 CrossRef Medline
46. Reddi, A. R., Jensen, L. T., Naranuntarat, A., Rosenfeld, L., Leung, E., Shah, R., and Culotta, V. C. (2009) The overlapping roles of manganese and Cu/Zn SOD in oxidative stress protection. *Free Radic. Biol. Med.* **46,** 154–162 CrossRef Medline
47. Cohen, A., Perzov, N., Nelson, H., and Nelson, N. (1999) A novel family of yeast chaperons involved in the distribution of V- ATPase and other membrane proteins. *J. Biol. Chem.* **274,** 26885–26893 CrossRef Medline
48. Aksoy, M., Pootakham, W., and Grossman, A. R. (2014) Critical function of a *Chlamydomonas reinhardtii* putative polyphosphate polymerase subunit during nutrient deprivation. *Plant Cell* **26,** 4214–4229 CrossRef Medline
49. Ruiz, F. A., Rodrigues, C. O., and Docampo, R. (2001) Rapid changes in polyphosphate content within acidocalcisomes in response to cell growth, differentiation, and environmental stress in *Trypanosoma cruzi*. *J. Biol. Chem.* **276,** 26114–26121 CrossRef Medline
50. Yu, D., Danku, J. M. C., Baxter, I., Kim, S., Vatamaniuk, O. K., Vitek, O., Ouzzani, M., and Salt, D. E. (2012) High-resolution genome-wide scan of genes, gene-networks and cellular systems impacting the yeast ionome. *BMC Genomics* **13,** 623 CrossRef Medline
51. Azevedo, C., and Saiardi, A. (2014) Functions of inorganic polyphosphates in eukaryotic cells: a coat of many colours. *Biochem. Soc. Trans.* **42,** 98–102 CrossRef Medline
52. Hothorn, M., Neumann, H., Lenherr, E. D., Wehner, M., Rybin, V., Hassa, P. O., Uttenweiler, A., Reinhardt, M., Schmidt, A., Seiler, J., Ladurner, A. G., Herrmann, C., Scheffzek, K., and Mayer, A. (2009) Catalytic core of amembrane-associated eukaryotic polyphosphate polymerase. *Science* **324,** 513–516 CrossRef Medline
53. Wang, Y., Weisenhorn, E., MacDiarmid, C. W., Andreini, C., Bucci, M., Taggart, J., Banci, L., Russell, J., Coon, J. J., and Eide, D. J. (2018) The cellular economy of the: *Saccharomyces cerevisiae* zinc proteome. *Metallomics* **10,** 1755–1776 CrossRef Medline
54. Merchant, S. S., Allen, M. D., Kropat, J., Moseley, J. L., Long, J. C., Tottey, S., and Terauchi, A. M. (2006) Between a rock and a hard place: trace element nutrition in Chlamydomonas. *Biochim. Biophys. Acta* **1763,** 578–594 CrossRef Medline
55. Lytle, F. W., Greegor, R. B., and Panson, A. J. (1988) Discussion of X-ray-absorption near-edge structure: application to Cu in the high-Tc superconductors La1.8Sr0.2CuO4 and YBa2Cu3O7. *Phys. Rev. B* **37,** 1550–1562 CrossRef
56. Bencze, K. Z., Kondapalli, K. C., and Stemmler, T. L. (2007) In *Applications of Physical Methods in Inorganic and Bioinorganic Chemistry: Handbook, Encyclopedia of Inorganic Chemistry* (Scott, R. A., and Lukehart, C. M., eds) pp. 513–528, John Wiley & Sons, Ltd., Chichester, UK
57. Bakthavatsalam, S., Sarkar, A., Rakshit, A., Jain, S., Kumar, A., and Datta, A. (2015) Tuning macrocycles to design 'turn-on' fluorescence probes for manganese(II) sensing in live cells. *Chem. Commun.* **51,** 2605–2608 CrossRef
58. Goodenough, U., Heiss, A. A., Roth, R., Rusch, J., and Lee, J. H. (2019) Acidocalcisomes: ultrastructure, biogenesis, and distribution in microbial eukaryotes. *Protist* **170,** 287–313 CrossRef Medline
59. Sharma, A., Gaidamakova, E. K., Grichenko, O., Matrosova, V. Y., Hoeke, V., Klimenkova, P., Conze, I. H., Volpe, R. P., Tkavc, R., Gostinčar, C., Gunde-Cimerman, N., DiRuggiero, J., Shuryak, I., Ozarowski, A., Hoffman, B. M., and Daly, M. J. (2017) Across the tree of life, radiation resistance is governed by antioxidant Mn^{2+}, gauged by paramagnetic resonance. *Proc. Natl. Acad. Sci. U.S.A.* **114,** E9253–E9260 CrossRef Medline
60. Haddy, A. (2007) EPR spectroscopy of the manganese cluster of photosystem II. *Photosynth. Res.* **92,** 357–368 CrossRef Medline
61. Cramer, C. L., and Davis, R. H. (1984) Polyphosphate-cation interaction in the amino acid-containing vacuole of *Neurospora crassa*. *J. Biol. Chem.* **259,** 5152–5157 Medline
62. Stich, T. A., Lahiri, S., Yeagle, G., Dicus, M., Brynda, M., Gunn, A., Aznar, C., Derose, V. J., and Britt, R. D. (2007) Multifrequency pulsed EPR studies of biologically relevant manganese(II) complexes. *Appl. Magn. Reson.* **31,** 321–341 CrossRef Medline
63. Culotta, V. C., Yang, M., and Hall, M. D. (2005) Manganese transport and trafficking: lessons learned from *Saccharomyces cerevisiae*. *Eukaryot. Cell* **4,** 1159–1165 CrossRef Medline
64. Rosenfeld, L., Reddi, A. R., Leung, E., Aranda, K., Jensen, L. T., and Culotta, V. C. (2010) The effect of phosphate accumulation on metal ion homeostasis in *Saccharomyces cerevisiae*. *J. Biol. Inorg. Chem.* **15,** 1051–1062 CrossRef Medline
65. Kropat, J., Hong-Hermesdorf, A., Casero, D., Ent, P., Castruita, M., Pellegrini, M., Merchant, S. S., and Malasarn, D. (2011) A revised mineral nutrient supplement increases biomass and growth rate in *Chlamydomonas reinhardtii*. *Plant J.* **66,** 770–780 CrossRef Medline
66. Gerasimaitė, R., Sharma, S., Desfougères, Y., Schmidt, A., and Mayer, A. (2014) Coupled synthesis and translocation restrains polyphosphate to acidocalcisome-like vacuoles and prevents its toxicity. *J. Cell Sci.* **127,** 5093–5104 CrossRef Medline
67. Moseley, J. L., Chang, C. W., and Grossman, A. R. (2006) Genome-based approaches to understanding phosphorus deprivation responses and PSR1 control in *Chlamydomonas reinhardtii*. *Eukaryot. Cell* **5,** 26–44 CrossRef Medline
68. Glaesener, A. G., Merchant, S. S., and Blaby-Haas, C. E. (2013) Iron economy in *Chlamydomonas reinhardtii*. *Front. Plant Sci.* **4,** 337 CrossRef Medline
69. Strenkert, D., Limso, C. A., Fatihi, A., Schmollinger, S., Basset, G. J., and Merchant, S. S. (2016) Genetically programmed changes in photosynthetic cofactor metabolism in copper-deficient chlamydomonas. *J. Biol. Chem.* **291,** 19118–19131 CrossRef Medline
70. Ghosal, S., Fallon, S. J., Leighton, T. J., Wheeler, K. E., Kristo, M. J., Hutcheon, I. D., and Weber, P. K. (2008) Imaging and 3D elemental characterization of intact bacterial spores by high-resolution secondary ion mass spectrometry. *Anal. Chem.* **80,** 5986–5992 CrossRef Medline
71. Slaveykova, V. I., Guignard, C., Eybe, T., Migeon, H.-N., and Hoffmann, L. (2009) Dynamic NanoSIMS ion imaging of unicellular freshwater algae exposed to copper. *Anal. Bioanal. Chem.* **393,** 583–589 CrossRef Medline
72. Chandra, S. (2010) Subcellular imaging of cells and tissues with dynamic secondary ion mass spectrometry. in *The Encyclopedia of Mass Spectrometry* (Gross, M., and Caprioli, R., eds) pp. 469–480, Elsevier, Amsterdam
73. Pett-Ridge, J., and Weber, P. K. (2012) NanoSIP: NanoSIMS applications for microbial biology. *Methods Mol. Biol.* **881,** 375–408 CrossRef Medline
74. Werst, M. M., Davoust, C. E., and Hoffman, B. M. (1991) Ligand spin densities in blue copper proteins by Q-band ^{1}H and N ENDOR spectroscopy. *J. Am. Chem. Soc.* 113, 1533–1538 CrossRef
75. Davoust, C. E., Doan, P. E., and Hoffman, B. M. (1996) Q-band pulsed electron spin-echo spectrometer and its application to ENDOR and ESEEM. *J. Magn. Reson. Ser. A* **119,** 38–44 CrossRef
76. Abragam, A., and Bleaney, B. (1970) *Electron Paramagnetic Resonance of Transition Ions*, Chapter 1, pp. 87–92, Oxford University Press, Oxford, UK
77. Hoffman, B. M. (2003) ENDOR of metalloenzymes. *Acc. Chem. Res.* **36,** 522–529 CrossRef Medline
78. Hoffman, B. M. (2003) Electron-nuclear double resonance spectroscopy (and electron spin-echo envelope modulation spectroscopy) in bioinorganic chemistry. *Proc. Natl. Acad. Sci. U.S.A.* **100,** 3575–3578 CrossRef Medline
79. Salikhov, K. M., Schweiger, A., and Jeschke, G. (2002) Principles of pulse electron paramagnetic resonance. *Appl. Magn. Reson.* **22,** 319–319 CrossRef